Aerodynamic Characterization of a Tethered Rotor

by

Piyush Hota

A Thesis Presented in Partial Fulfillment
of the Requirements for the Degree
Masters of Science

Approved November 2019 by the
Graduate Supervisory Committee:

Valana Wells, Chair
Ronald Calhoun
Frederick Garrett

ARIZONA STATE UNIVERSITY

December 2019

ABSTRACT

An airborne, tethered, multi-rotor wind turbine, effectively a rotorcraft kite, provides one platform for accessing the energy in high altitude winds. The craft is maintained at altitude by its rotors operating in autorotation, and its equilibrium attitude and dynamic performance are affected by the aerodynamic rotor forces, which in turn are affected by the orientation and motion of the craft. The aerodynamic performance of such rotors can vary significantly depending on orientation, influencing the efficiency of the system. This thesis analyzes the aerodynamic performance of an autorotating rotor through a range of angles of attack covering those experienced by a typical autogyro through that of a horizontal-axis wind turbine. To study the behavior of such rotors, an analytical model using the blade element theory coupled with momentum theory was developed. The model uses a rigid-rotor assumption and is nominally limited to cases of small induced inflow angle and constant induced velocity. The model allows for linear twist. In order to validate the model, several rotors – off-the-shelf model-aircraft propellers – were tested in a low speed wind tunnel. Custom built mounts allowed rotor angles of attack from 0 to 90 degrees in the test section, providing data for lift, drag, thrust, horizontal force, and angular velocity. Experimental results showed increasing thrust and angular velocity with rising pitch angles, whereas the in-plane horizontal force peaked and dropped after a certain value. The analytical results revealed a disagreement with the experimental trends especially at high pitch angles. The discrepancy was attributed to the rotor operating in turbulent wake and vortex ring states at high pitch angles, where momentum theory has proven to be invalid. Also, aerodynamic design constants, which are not precisely known for the test propellers, have an underlying effect on the analytical model. The developments of the thesis suggest that a different analytical model may be needed for high rotor angles of attack. However, adding a term for resisting torque to the model gives analytical results that are similar to the experimental values.

ACKNOWLEDGEMENTS

Foremost, I would like to extend my sincere gratitude to my faculty advisor and chair Dr. Valana Wells for her continuous support, patience and motivation. She played an extensive role to transform my rudimentary conjectures into this structured research. I would also like to thank my committee members Dr. Ronald Calhoun and Dr. Frederick Garrett for expanding my thought process. My heartfelt gratitude to Dr. Bruce Steele, for his unflinching help and co-operation during the experimental work at the wind tunnel facility. Thanks to Mr. Leonard Bucholz for all the manufacturing work at the SEMTE Student Machine Shop. Most importantly, my deepest appreciation to my parents and Mahima, for their unfailing support and understanding. Without them I never would have been able to pursue my passion and advance my education.

TABLE OF CONTENTS

LIST OF TABLES

LIST OF FIGURES

Chapter 1

INTRODUCTION

In addition to their functionality for producing lift and thrust on flying vehicles, rotating wings have proven effective for extracting energy from the motion of the atmosphere. Wind energy has become the most comprehensive and mature type of intermittent renewable power. The installed capacity of wind in the United States by the end of second quarter, 2019 was at 97,960 MW [1]. Wind energy has enormous potential for further development. However, conventional wind turbines have drawbacks, such as saturation of inland windy areas, bird and bat mortality, noise, aesthetic impacts, and fitful wind speeds.

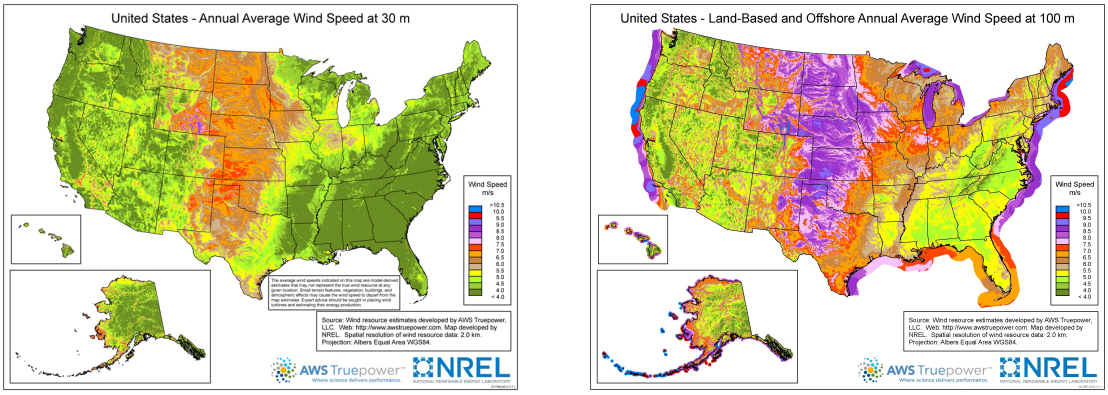

(a). 30m altitude (b). 100m altitude

Figure 1. United States Average Annual Wind Speed [2]

It has been a known fact that the wind speed increases with height from the surface to the upper troposphere. There are several reasons associated with this tendency. Firstly, the horizontal pressure gradient increases with height. The height of the troposphere is taller in warmer air, since warm air is less dense and thus occupies a greater volume. Going up in altitude, the pressure gradient between the warm

and cold air increases with height. This results in a greater pressure gradient, thus stronger wind. Secondly, the wind speed is lower near the ground due to surface friction. Surface objects such as trees, rocks, houses, etc. slow the air as it collides into them. The influence of this friction is less with height above the ground, thus the wind speed increases with height. Lastly, the density of the air is highest at the surface and decreases with height. A force imparted on air will move the air more easily when the mass of the air is lesser. Denser air requires a greater force to make it flow. With air density decreasing with height, the lower density air flows with a relatively higher speed. Figure 1 (a) and 1 (b) show the average wind speeds at 30m and 100m altitude respectively in the United States. At the higher altitude the wind speeds are observed to be significantly higher. Also, a typical profile of wind speed variation with altitude is shown in Figure 2.

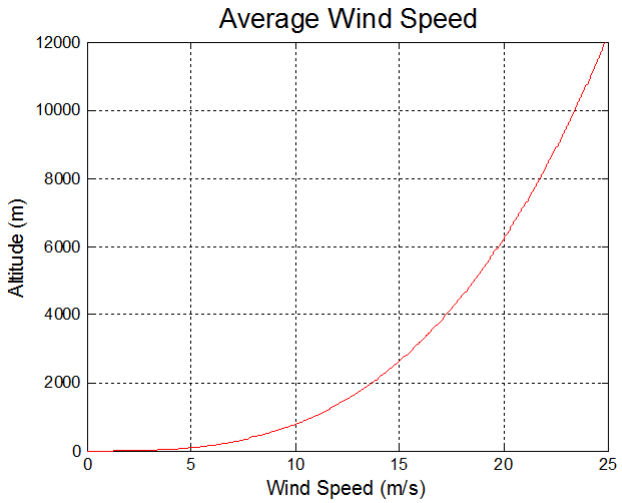

Figure 2. A Typical Wind Speed Profile [3]

The power available in wind is generally given by the formula $P = 0.5\rho AV_{\infty}^{3}$. This implies that even a small increase in velocity can have a large positive effect on the available power. Therefore, if power could be extracted at higher altitudes, a lot more power can be gained with the same area of blades, or by reducing the diameter of blades to a large extent. Airborne wind turbines are machines that operate on this

idea to harness high altitude wind power. Most airborne wind turbines are effectively a kite tethered to the ground. Airborne wind turbines are broadly classified as ground based generators and airborne generators. The later type can be like an aircraft or drone carrying an on-board generator which can tap high velocity winds and convert the rotational energy to electrical energy. The energy can then be transmitted to the ground through the tether. A great advantage in this scenario is the relatively high wind velocity avoids the use of gearboxes which contributes to a required light weight design. The alluring feature about this system is the on-board generator that can be switched to act as a motor during take off and landing. The turbines can act as propellers to produce thrust to maneuver the aircraft to the ground, or vice versa. A particular development here, classified in the category of airborne generators, is a tethered rotor-craft concept or also called the "Flying Electric Generator". This concept, based on autorotation was introduced and developed from the late 1970's by Robert and Shepard [4]. The tethered rotorcraft is variation of the an autogyro, where the rotors concurrently extract power and produce lift to keep the kite airborne.

1.1 Autorotation

Autorotation is a common phenomenon experienced by helicopters where the vehicle's rotors generate lift by rotating as its loses altitude. Leishman [5] defines autorotation as a self sustained rotation of the rotor without the application of any shaft torque ($Q = 0$). The energy to drive the rotor comes from conversion of potential energy to kinetic energy from the descending rotor. The phenomenon of autorotation had been first observed in nature with the sycamore seeds when they free fall. The first application of autorotation was developed by Juan de la Cierva in 1920 with the autogyro. Since then the phenomenon has been used for helicopters, and other advancements in autogyro.

To begin with, the basics physics behind the operation of this system is discussed. In general, for rotors, the actuator disk setup using the momentum theory has been

the simplest principle used to model rotors. Using the standard helicopter rotor terminology for a rotor in ascent, the stream velocity direction points downwards. Applying the control volume analysis, we can define the ratio of induced velocity to hover induced velocity as

$$\frac{\nu_i}{\nu_h} = -\left(\frac{V_c}{2\nu_h}\right) \pm \sqrt{\left(\frac{V_c}{2\nu_h}\right)^2 + 1} \tag{1.1}$$

During descent, the direction of slipstream velocity changes, along with the direction of induced velocity changes. Hence, we have,

$$\frac{\nu_i}{\nu_h} = -\left(\frac{V_c}{2\nu_h}\right) \pm \sqrt{\left(\frac{V_c}{2\nu_h}\right)^2 - 1} \tag{1.2}$$

Where, ν_i is the average induced velocity, ν_h is the hover induced velocity and V_c is the climb velocity. The above equation for descend is only valid for V_c being than twice the average induced velocity at disk [5]. Plotting these equations for a range of velocity ratios would have a plot as shown in Figure 3.

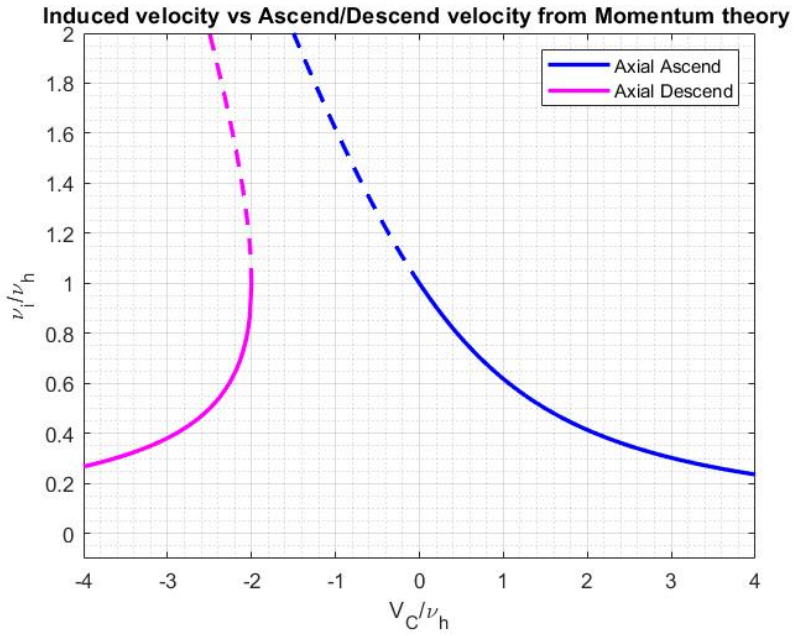

Figure 3. Induced Velocity vs Stream Velocity

The curve in pink represents the windmill brake state, and the curve in blue represents the normal working state of a helicopter in climb. The dashed curves represent the extension of the axial climb state into negative velocities or the descend state with the other solution of the quadratic equation above. The dashed curves violate the assumed direction of flow, hence may be treated as an unviable solution. As originally suggested by Hafner [6] and Lock [7], the state between descend velocities between $-2\nu_h$ and 0, can a have a slipstream in any direction. As there is no definite control volume that can be applied to the region, the momentum theory fails to apply. Leishman [5] states that the velocities in this region gets difficult to define even empirically as the rotor tip interactions makes the flow unsteady and turbulent. This state is usually defined as the Vortex Ring State. This usually occurs when a helicopter begins to descend vertically and continues to descend at a high rate till it reaches the windmill brake state. Approaching this region, the induced velocities in the center change direction with the high rate of descend. In the vortex ring state, the upward and downward velocities start interacting and causing circulation along the span of the blade. This can cause a severely loss of lift, as the power from the rotor is just used to form the vortexes. If the rotor continues to descend at higher rate, crossing the turbulent wake region it finally enters the wind brake state. The point between the two regions is where the ideal autorotation lies.

1.2 Momentum Theory Validity

Figure 4 shows the working states of a general rotor in axial flight. Typically the state of autorotation lies between the region $-2 \leq V_c/\nu_h \leq 0$, where the classical momentum theory fails to apply directly, as also shown in Figure 3. Leishman [5] also defines a region of a ideal autorotation where $V_c + \nu_i = 0$. This is region where 0 net power is required by the rotor.

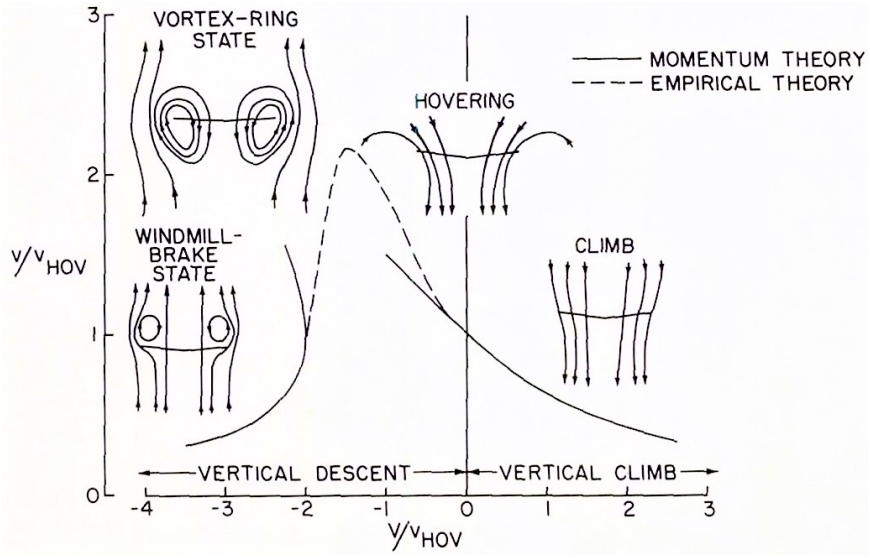

Figure 4. Working States of Rotor in Axial Flight [8]

In general, investigators studying these conditions from the wind-energy perspective, utilize a different terminology, including the idea of the axial flow factor. To understand better, the following discussion will bridge the helicopter terminology to the wind turbine terminology.

The axial induction factor is defined as,

$$a = \frac{\text{Induced velocity at rotor}}{\text{Free stream velocity}} = \frac{V_\infty - V_{disk}}{V_\infty}$$

Comparing the above equation to the axial induced velocity of a helicopter, ν_i would be negative, as wind turbine terminology assumes a positive velocity in the downstream direction. V_c now represents the free stream velocity.

$$a = \frac{-\nu_i}{V_c} = \frac{-\nu_i}{V_c}\frac{\nu_h}{\nu_h} = \frac{-\nu_i/\nu_h}{V_c/\nu_h}$$

As discussed earlier, autorotation typically would occur in the region $-2 \leq V_c/\nu_h$, and the point of ideal autorotation $V_c + \nu_i = 0$. Therefore, evaluating this region in terms of axial induction factor.

- $V_c/\nu_h = -2$

  Since momentum theory is valid for descend in this region, using equation 1.2,

$$\frac{\nu_i}{\nu_h} = -\left(\frac{V_c}{2\nu_h}\right) \pm \sqrt{\left(\frac{V_c}{2\nu_h}\right)^2 - 1} = -\left(\frac{-2}{2}\right) \pm \sqrt{\left(\frac{-2}{2}\right)^2 - 1}$$

$$\frac{\nu_i}{\nu_h} = 1$$

  Therefore,

$$a = \frac{-\nu_i/\nu_h}{V_c/\nu_h} = \frac{-1}{-2}$$

$$a = 0.5$$

- $V_c/\nu_h = 0$

  Similarly at the point of ideal autorotation, $V_c = -\nu_i$

$$a = \frac{-\nu_i}{V_c} = \frac{-\nu_i}{-\nu_i}$$

$$a = 1$$

Hence, with the above deductions, we can say that autorotation primarily occurs in the region, $0.5 \leq a \leq 1$. Eggleston and Stoddard [9], illustrated a plot (Figure) depicting the coefficient of thrust vs axial induction factor for the momentum theory. The normal windmill operating stage is valid in the region of $0 < a < 0.5$. The region of $a < 0$ refers to the normal operating stage of a propeller or helicopter, where power is being supplied to the rotor.

When the axial induction factor is greater than 0.5, the rotor encounters the turbulent wake state, where momentum theory has proved to be invalid (denoted by dashed line). Reverse flow regions encountered here, tend to increase the axial induction factor and force the rotor into the vortex ring state. Early, experimental results by Glauert [11], and Lock [12], have show that thrust tends to increase in the region from $0.5 \leq a \leq 1$. The symbols on the plot denote experimental data

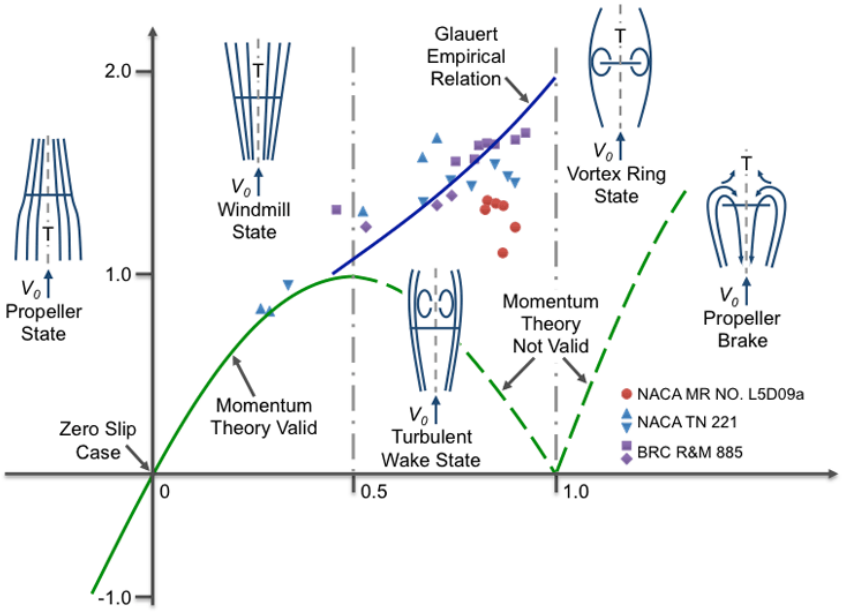

Figure 5. Validity of Momentum Theory [10]

by Glauert. The abrupt increase of the coefficient of thrust after a greater than 0.4 can be associated with flow separation and stall. Glauert suggests and empirical relationship at about $a = 0.4$, that connects the curve from the momentum theory to the limiting value of coefficient of thrust. $C_T = 2$ represents the drag coefficient of a flat plate perpendicular to the flow [10].In 2005, Buhl [13] suggests that C_T is simply not a function of the axial induction factor in the turbulent wake state because there is a wide spread in experimental data in comparison to the analytical expressions. He develops a new quadratic relation which reduces the discontinuity at $C_T \approx 0.4$. Various researchers have attempted to improve the empirical relationship for the turbulent wake state or vortex ring state, but none are associated with physical realization of thrust increasing in the flow state.

1.3 Autorotation Model Literature Survey

As explained in the previous section, autorotation lies in the region where momentum theory is invalid, hence cannot be directly modeled with it. Glauert [14] initially modeled an autorotating rotor by coupling the blade element theory with momentum

theory. Importantly the inflow was based on the momentum theory. This method is still largely used today for modeling of autogyros rotors.

In 1928, Glauert[14] developed a model based on the assumption that the angles of incidence on each blade element are small that the interference flow is similar to that caused by an ordinary airfoil. With this fact he ignores the higher order harmonics in his analysis. Using an average axial induced velocity, constant chord and fixed uniform pitch he derives the coefficient of thrust, horizontal force and torque coefficients, and solves the equations to determine the coefficient of lift and drag. He concludes that the coefficient of lift non-dimensionalized by the free stream velocity is maximized at 0.5 to 0.6. The maximum lift to drag is in the ratio of 6 to 8.

Wheatley [15] extends Glauert's and Lock's theory by introducing variable pitch along with the inclusion of the effect of blade tip losses and influence of reversed velocities on retreating blades. He shows that the induced velocity has a secondary effect on the net rotor forces, wheres the effect of flapping is substantial. He discusses how the consideration of uniform induced velocity affects the analysis at low and high tip speed ratios. He inherently specifies to use two different methods for analysis, one for low incidence and for high incidence.

Setter and Rosen [16] investigate a steady state axial motion of autorotation for rotary decelerators. Their initial parametric study theoretically and experimentally show the aerodynamics for a generalised auto-rotating rotor. Concerning this thesis, the most important take away from their research is the flow states for autorotation. They base the relationship between the normalized induced velocity and the normalized descent velocity for the vortex ring state and windmill brake state. It is also suggested that the inner cross sections of the blades experience relatively high angles of attack, and these cross sections tend to experience stall and are not dealt by simplified models. Each elemental cross-sectional properties influence the state of steady autorotation. They conclude on the fact that in order to accurately model theoretical steady

autorotation, a definite database of aerodynamic characteristics at each cross-section is required.

Rimkus and Das [17], applied an aerodynamic analyses of the autogyro for airborne wind energy extraction applications. The configuration of the device is very similar the one introduced by Robert [4]. Rimkus and Das, model the energy extraction as an additional braking torque. The results depicted with steady state conditions are developed with specific parameters for a particular rotor. The results show various aerodynamic performance parameters as function of angle of incidence for both an ideal autogyro and an airborne wind turbine.

The work by Kentfield and Brophy [18], explore another application of application with the theory of Cierva-Rotor Wind turbines. To maximize power production a wind turbine rotor is tilted 40° to 50° relative to the vertical. The author develops a custom code called CIERVACALC to model massively tangential flow conditions. The code customizes the classical Glauert's theory to apply to an modified actuator disc on elliptical cross-section.Azimuthal variations in the flow are accounted for in the code. The results show a equivalent match, when the angle is set to operate as a horizontal axis wind turbine. Also, the code imbibes static flat plate aerodynamic drag coefficient characteristics for high angles of attack. The authors, conclude with discussing the advantages of the configuration of not having flap-wise bending moments under running conditions, ground level yaw system and lowering of turbines during dangerous hurricanes.

1.4 Characterizing Autorotation for Highly Pitched Rotors

In regards to all the applications and discussions above, this thesis aims to model autorotation for a range of pitch angles, from the state of a helicopter or autogyro rotor to a horizontal axis wind turbine. The thesis includes both an analytical derivation and an experimental study. The analytical study extends Glauert's theory of the autogyro [14], including higher-order terms in advance ratio and higher rotor angles of attack.

A linear twist is also introduced into the model. A hingeless rotor without flapping will be assumed to simplify the model and provide a comparison to the experimented rotors. To understand the aerodynamic performance of practical autorotating rotors, various experiments are conducted in a low speed wind tunnel. The experiments measure the lift, drag, thrust and horizontal force. The effects of blade pitch are evaluated on the basis of the experimental results. A comparison is made between the analytical and experimental results. Lastly, an explanation is offered for how the effects of flow states affect the analytical results for an autorotating rotor.

Chapter 2

DEVELOPMENT OF AN ANALYTICAL MODEL FOR ROTOR THRUST

A rotor operating in the state of autorotation can develop significant thrust in order to sustain flight. In this chapter we will investigate the derivation of thrust and horizontal forces of a rotor in autorotation using the blade element momentum theory, as introduced by Glauert [14]. It has been a successful tool in analyzing all kinds of rotors. The theory combines the momentum theory to the blade element theory. Blade Element theory breaks down the rotor into multiple elements, computing the elemental forces acting on a quasi-static 2D element. The rotor performance parameters can then be obtained by integrating over the entire length and averaging about the entire azimuth. For this analysis we will assume that the angles of incidence of relative velocity on a blade element are small and we have no flapping at the rotor hinge. In simple sense it can be considered as a hingeless rotor. This work below will be used to develop an analysis of the rotor parameters for autorotation.

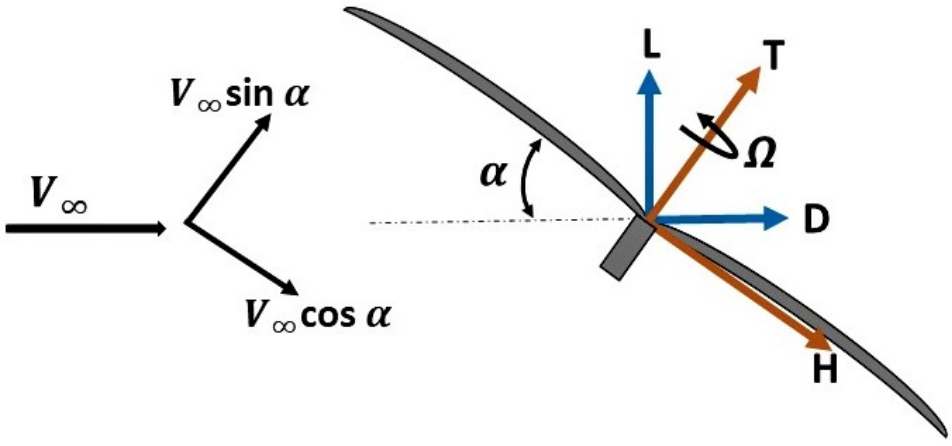

Figure 6. Incoming Flow on an Auto-Rotating Rotor

Consider a rotor of radius R with N_b blades, which rotate at an angular velocity of Ω. The case is similar to a forward flight condition of rotor, but instead we have an

oncoming wind at a velocity V_∞ as shown in Figure 6. The rotor is inclined backward to the horizontal wind at an angle α to the horizontal. This is exhibiting the condition of autorotation. The shaft is normal to the plane of rotation. The free stream velocity will act in two directions, along the rotor axis and along the rotor plane outwards as shown. The radial component component of velocity will be ignored, for clarity and ease. In reality there are multiple complications due to flapping, compressibility effects, unsteady effects, non linear aerodynamics, stall and reverse flow. These are difficult to model and often complicate the process of derivation.

The advance ratio (μ),and induced inflow ratio are defined as, respectively:

$$\mu = \frac{V_\infty}{\Omega R} \qquad\qquad \lambda_i = \frac{\nu_i}{\Omega R}$$

where, ν_i is the induced velocity at the rotor. As discussed later, we assume an average induced velocity for the entire rotor. In reality the induced velocity varies over the entire span of the blade.

In forward flight, the rotor thrust is given by the relation [14],

$$\begin{aligned} T &= 2(\rho A V')\nu_i \\ &= 2\rho A \nu_i \sqrt{(V_\infty \cos\alpha)^2 + (V_\infty \sin\alpha - \nu_i)^2} \end{aligned}$$

where, A is the area of the rotor disk, ρ is the density of air, and V' is the resultant velocity experienced by the rotor. Rearranging and non-dimensionalizing both sides by $(\Omega R)^2$.

$$\begin{aligned} \frac{T}{2\rho A(\Omega R)^2} &= \frac{\nu_i}{\Omega R} \frac{\sqrt{(V_\infty \cos\alpha)^2 + (V_\infty \sin\alpha - \nu_i)^2}}{\Omega R} \\ &= \frac{\nu_i}{\Omega R} \sqrt{\left(\frac{V_\infty}{\Omega R}\cos\alpha\right)^2 + \left(\frac{V_\infty}{\Omega R}\sin\alpha - \frac{\nu_i}{\Omega R}\right)^2} \end{aligned}$$

$$\frac{C_T}{2} = \lambda_i \sqrt{(\mu\cos\alpha)^2 + (\mu\sin\alpha - \lambda_i)^2}$$

where, the dimensionless thrust coefficient is given by,

$$C_T = \frac{T}{\rho A(\Omega R)^2}$$

Therefore,

$$\lambda_i = \frac{C_T}{2\sqrt{(\mu\cos\alpha)^2 + (\mu\sin\alpha - \lambda_i)^2}} \tag{2.1}$$

Now defining the total inflow ratio as,

$$\lambda = \mu\sin\alpha - \lambda_i \tag{2.2}$$

Equation 2.1 can be expressed as,

$$\lambda_i = \frac{C_T}{2\sqrt{(\mu\cos\alpha)^2 + \lambda^2}}$$

Hence, we have,

$$\lambda = \mu\sin\alpha - \frac{C_T}{2\sqrt{(\mu\cos\alpha)^2 + \lambda^2}} \tag{2.3}$$

This is one of the most important equations obtained, and will be referenced later on. It must be noted, this a result is derived on the basis of the momentum theory.

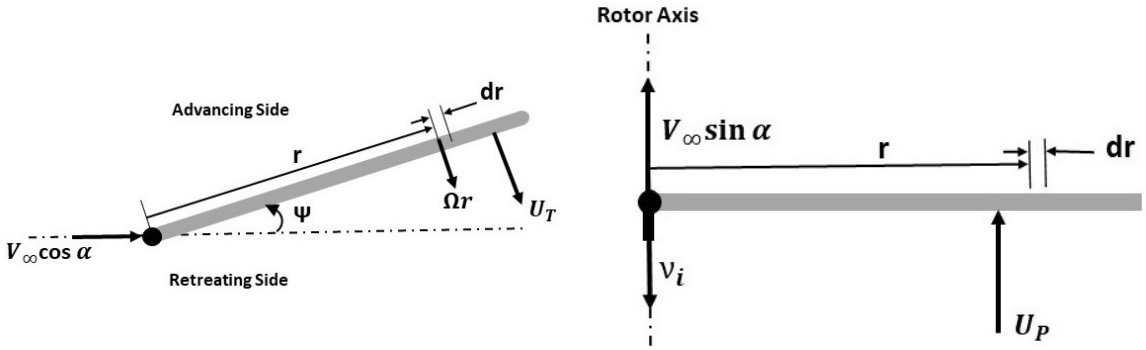

(a). Top view along the rotor axis (b). Front view along the rotor plane

Figure 7. Incident Velocities on Blade

As sketched in Figure 7 (a) the rotor elements encounter a tangential velocity which is a combination of two velocities: one from the oncoming flow which eventually becomes a function of the azimuth and, secondly, the linear velocity originating from

the angular rotation of the rotor. ΩR is defined such that it is the oncoming velocity to the rotor. Similarly, when looked at from the hub plane as shown in Figure 7 (b), the perpendicular velocity is a combination of the component of the free-stream velocity perpendicular to the rotor plane and the induced velocity. Due to the forces exerted on the rotor, the undisturbed flow in the vicinity is affected which gives rise to local induced velocities. The complexity of flow makes it difficult to solve for a non-uniform induced velocity over the rotor. To develop a relatively simple model we will assume a constant induced velocity over the entire length [19].

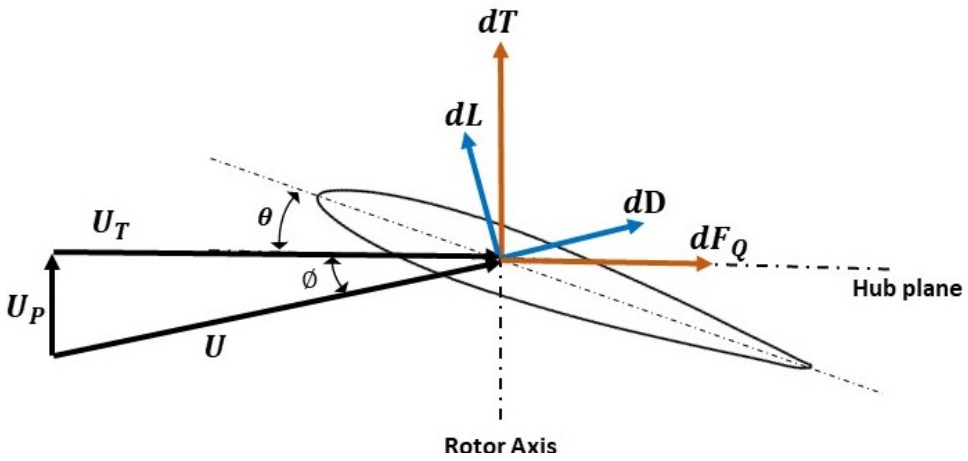

Figure 8. Aerodynamic Environment at a Typical Blade Element

Figure 8 shows a diagrammatic representation of the forces on a blade element. The relative velocity U is shown, which is a combination of U_T and U_P. θ depicts the blade pitch angle, usually measured at 75% radial length. The first analysis will assume a constant pitch over the radial length, but a linear twist will be introduced later. The relative inflow angle ϕ is produced primarily due to the the induced velocity by the rotor and the wake. Therefore, the induced velocity serves to adjust the angle of the relative flow velocity vector and so modifies the angle of attack at each blade element from its two dimensional value [5]. In the process of deriving, ϕ will later be considered as a small angle. The angle of attack for a rotor element can therefore be defined as, $\alpha_b = \theta + \phi$. For ease, the chord length of c has been presumed to be

constant for each blade. The shape of the blade will be assumed having simple form in subsequent analysis. As described in the figure, dL is the elemental lift, dD is the elemental drag. The elemental thrust is denoted by dT, while the elemental force for torque is named dF_Q. By geometry, the thrust and torque force can be resolved as,

$$dT = dL\cos\phi + dD\sin\phi$$
$$dF_Q = -dL\sin\phi + dD\cos\phi \tag{2.4}$$

The velocities can be established as,

$$U = \sqrt{U_T^2 + U_P^2} \tag{2.5}$$
$$U^2 = U_T^2 + U_P^2$$

$$U_T = U\cos\phi = V_\infty\cos\alpha\sin\psi + \Omega r \qquad U_P = U\sin\phi = V_\infty\sin\alpha - \nu_i \tag{2.6}$$

Note that the induced velocity is opposite to the $\hat{e_p}$ axis. The non-dimensionalized radial distance ($\bar{r}$) is defined as, $\bar{r} = r/R$.

Expanding the square of dimensionless tangential and perpendicular velocity as,

$$\begin{aligned}\frac{U_T^2}{(\Omega R)^2} &= \frac{V_\infty^2}{(\Omega R)^2}\cos^2\alpha\sin^2\psi + \frac{\Omega^2 r^2}{(\Omega R)^2} + 2\frac{V_\infty}{(\Omega R)}\sin\psi\frac{\Omega r}{(\Omega R)} \\ &= \mu^2\cos^2\alpha\sin^2\psi + \bar{r}^2 + 2\mu\cos\alpha\sin\psi\bar{r}\end{aligned} \tag{2.7}$$

$$\frac{U_P}{(\Omega R)} = \frac{V_\infty}{(\Omega R)}\sin\alpha - \frac{\nu_i}{\Omega R} = \mu\sin\alpha - \lambda_i = \lambda \tag{2.8}$$

As defined by equation 2.2. Therefore,

$$\frac{U_P^2}{(\Omega R)^2} = (\mu\sin\alpha - \lambda_i)^2 = \lambda^2 \tag{2.9}$$

To develop an analytical equation, we must assume small angle ϕ assumptions, in order to integrate non-numerically. These assumptions break down over the root of the blade and over a wide range of retreating blades, since the angle ϕ discontinues to

be small [14]. Glauert suggests the tangential velocity component U_T must be positive over the outer half of the retreating blade. He sets the limiting parameter as,

$$\mu \cos \alpha < \frac{1}{2}$$

With a small ϕ assumption, it can be assumed that, $U \approx U_T$, $\cos \phi \approx 1$ and $\sin \phi \approx \phi$. Geometrically, ϕ can be defined as,

$$\phi = tan^{-1} \frac{U_P}{U_T}$$

But, with the small angle assumption, we can say

$$\phi \approx \frac{U_P}{U_T} \tag{2.10}$$

The elemental Lift and Drag can be defined to determine Thrust, Horizontal Force, and Torque in the subsequent sections. It can be given as,

$$dL = \frac{1}{2} \rho U^2 c C_l dr$$
$$dD = \frac{1}{2} \rho U^2 c C_d dr$$

The coefficient of lift of an airfoil section corresponds to two dimensional motion at the angle of incidence. It is related as,

$$C_l = C_{l\alpha} \alpha_b = C_{l\alpha}(\theta + \phi)$$

where, $C_{l\alpha}$ is the lift curve slope, and θ is the pitch of airfoil cross-section. For simplicity we will assume an average lift curve slope $C_{l\alpha}$ for the entire rotor. Lastly, the solidity ratio of a rotor is defined as the ratio of blade area to disk area. It is an important design parameter for rotors.

$$\sigma = \frac{N_b c R}{\pi R^2} = \frac{N_b c}{\pi R}$$

2.1 Thrust Force

The total elemental thrust and elemental thrust coefficient as previously established is,

$$dT = N_b dL \cos\phi + N_b dD \sin\phi$$

$$dC_T = \frac{dT}{\rho A(\Omega R)^2} = dC_{TL} + dC_{TD}$$

The lift component of thrust coefficient can be hence put forward as,

$$\begin{aligned} dC_{TL} &= \frac{dT_L}{\rho A(\Omega R)^2} = \frac{dT_L}{\rho(\pi R^2)(\Omega^2 R^2)} = \frac{1}{2}\frac{N_b c}{\pi R}\frac{\rho}{\rho}C_l\frac{dr}{R}\cos\phi \\ &= \frac{1}{2}\sigma\frac{U^2}{(\Omega R)^2}C_l d\bar{r}\cos\phi \end{aligned} \tag{2.11}$$

Similarly the drag component of thrust coefficient can be derived as,

$$dC_{TD} = \frac{dT_D}{\rho A(\Omega R)^2} = \frac{1}{2}\sigma\frac{U^2}{(\Omega R)^2}C_d d\bar{r}\sin\phi \tag{2.12}$$

To evaluate the total thrust coefficients, the differential coefficients must be integrated over the entire azimuth from 0 to 2π, and also over the complete radial distance of the blade from 0 to 1.

2.1.1 Lift Component

The Lift component of thrust can therefore be integrated as,

$$C_{TL} = \frac{1}{2\pi}\int_0^1\int_0^{2\pi} dC_{TL}\ d\psi\ d\bar{r} \tag{2.13}$$

$$\begin{aligned} C_{TL} &= \frac{1}{2\pi}\int_0^1\int_0^{2\pi}\frac{1}{2}\sigma\frac{U^2}{(\Omega R)^2}C_l\cos\phi\ d\psi\ d\bar{r} \\ &= \frac{1}{4\pi}\sigma\int_0^1\int_0^{2\pi}\frac{U^2}{(\Omega R)^2}C_l\cos\phi\ d\psi\ d\bar{r} \end{aligned}$$

Hence, with the small ϕ assumption,

$$\begin{aligned} C_{TL} &= \frac{1}{4\pi}\sigma\int_0^1\int_0^{2\pi}\frac{U_T^2}{(\Omega R)^2}C_{l\alpha}(\theta+\phi)\ d\psi\ d\bar{r} \\ &= \frac{1}{4\pi}\sigma C_{l\alpha}\left(\int_0^1\int_0^{2\pi}\frac{U_T^2}{(\Omega R)^2}\theta\ d\psi\ d\bar{r} + \int_0^1\int_0^{2\pi}\frac{U_T^2}{(\Omega R)^2}\phi\ d\psi\ d\bar{r}\right) \end{aligned}$$

Substituting above equation with equation 2.10, we have

$$C_{TL} = \frac{1}{4\pi}\sigma C_{l\alpha}\left(\int_0^1\int_0^{2\pi}\frac{U_T^2}{(\Omega R)^2}\theta\ d\psi\ d\bar{r} + \int_0^1\int_0^{2\pi}\frac{U_T^2}{(\Omega R)^2}\frac{U_P}{U_T}\ d\psi\ d\bar{r}\right)$$
$$= \frac{1}{4\pi}\sigma C_{l\alpha}\left(\theta\int_0^1\int_0^{2\pi}\frac{U_T^2}{(\Omega R)^2}\ d\psi\ d\bar{r} + \int_0^1\int_0^{2\pi}\frac{U_T U_P}{(\Omega R)^2}\ d\psi\ d\bar{r}\right)$$

By equation 2.7 and equation 2.9, the above would reduce to,

$$C_{TL} = \frac{1}{4\pi}\sigma C_{l\alpha}\Bigg(\theta\int_0^1\int_0^{2\pi}(\mu^2\cos^2\alpha\sin^2\psi + \bar{r}^2 + 2\mu\cos\alpha\sin\psi\ \bar{r})\ d\psi\ d\bar{r}$$
$$+\int_0^1\int_0^{2\pi}(\mu\cos\alpha\sin\psi + \bar{r})\ \lambda\ d\psi\ d\bar{r}\Bigg)$$

$$C_{TL} = \frac{1}{4\pi}\sigma C_{l\alpha}\left[\theta\ \frac{\pi}{3}\ (3\mu^2\cos^2\alpha + 2) + \pi\lambda\right]$$
$$= \frac{1}{12}\sigma C_{l\alpha}\ (3\theta\mu^2\cos^2\alpha + 2\theta + 3\lambda)$$

2.1.2 Drag Component

The Drag component even though not significant in comparison to the Lift component, can be solved as,

$$C_{TD} = \frac{1}{2\pi}\int_0^1\int_0^{2\pi} dC_{TD}\ d\psi\ d\bar{r} \tag{2.14}$$

$$C_{TD} = \frac{1}{2\pi}\int_0^1\int_0^{2\pi}\frac{1}{2}\sigma\frac{U^2}{(\Omega R)^2}C_d\sin\phi\ d\psi\ d\bar{r}$$
$$= \frac{1}{4\pi}\sigma C_d\int_0^1\int_0^{2\pi}\frac{U^2}{(\Omega R)^2}\sin\phi\ d\psi\ d\bar{r}$$

With the small ϕ assumption,

$$C_{TD} = \frac{1}{4\pi}\sigma C_d\int_0^1\int_0^{2\pi}\frac{U_T^2}{(\Omega R)^2}\phi\ d\psi\ d\bar{r}$$

Substituting above equation with equation 2.10, we have

$$C_{TD} = \frac{1}{4\pi}\sigma C_d\int_0^1\int_0^{2\pi}\frac{U_T^2}{(\Omega R)^2}\frac{U_P}{U_T}\ d\psi\ d\bar{r}$$
$$= \frac{1}{4\pi}\sigma C_d\int_0^1\int_0^{2\pi}\frac{U_T U_P}{(\Omega R)^2}\ d\psi\ d\bar{r}$$

By equation 2.7 and equation 2.9, the equation would reduce to,

$$\begin{aligned} C_{TD} &= \frac{1}{4\pi}\sigma C_d \int_0^1 \int_0^{2\pi} (\mu \cos\alpha \sin\psi + \bar{r})\lambda \; d\psi \; d\bar{r} \\ &= \frac{1}{4\pi}\sigma C_d[\pi\lambda] \\ &= \frac{1}{4}\sigma C_d \lambda \end{aligned}$$

The thrust coefficient is therefore,

$$\begin{aligned} C_T &= C_{TL} + C_{TD} \\ &= \frac{1}{12}\sigma C_{l\alpha} \; (3\theta\mu^2 \cos^2\alpha + 2\theta + 3\lambda) + \frac{1}{4}\sigma C_d \lambda \\ C_T &= \frac{1}{12}\sigma \left[C_{l\alpha} \; (3\theta\mu^2 \cos^2\alpha + 2\theta + 3\lambda) + 3C_d\lambda\right] \end{aligned} \tag{2.15}$$

2.2 Horizontal Force

The horizontal or H-force is the rotor-produced force acting in the plane of the rotor and, nominally, in the direction opposing the oncoming flow. [14]. For a helicopter or autogyro, the H-force is also known as the rotor drag. Mathematically we can define it as,

$$dH = N_b dD \cos\phi \sin\psi - N_b dL \sin\phi \sin\psi$$

Breaking down the two parts, such that

$$\begin{aligned} dH_{pr} &= \frac{1}{2} N_b \rho U^2 C_d dr \cos\phi \sin\psi \\ dH_{ind} &= \frac{1}{2} N_b \rho U^2 C_l dr \sin\phi \sin\psi \end{aligned}$$

The first part can defined as the profile component which arises due to from frictional resistance of the blades passing through the air, while the second is the induced component, incurred as a result of production of lift. The horizontal force coefficient can therefore be defined as,

$$dC_H = \frac{dH}{\rho A(\Omega R)^2} = dC_{Hpr} - dC_{Hind}$$

The Profile Horizontal coefficient is,

$$dC_{Hpr} = \frac{dH_{pr}}{\rho A(\Omega R)^2} = \frac{1}{2}\sigma\frac{U^2}{(\Omega R)^2}C_d d\bar{r}\cos\phi\sin\psi \tag{2.16}$$

The Induced Horizontal coefficient can be expanded as,

$$dC_{Hind} = \frac{dH_{ind}}{\rho A(\Omega R)^2} = \frac{1}{2}\sigma\frac{U^2}{(\Omega R)^2}C_l d\bar{r}\sin\phi\sin\psi \tag{2.17}$$

Similarly, to determine the total horizontal force coefficient the differential coefficients must be integrated over the entire azimuth from 0 to 2π and over the complete radial distance from 0 to 1.

2.2.1 Profile Drag Component

The profile drag horizontal force coefficient can therefore be integrated as,

$$C_{Hpr} = \frac{1}{2\pi}\int_0^1\int_0^{2\pi} dC_{Hpr}\ d\psi\ d\bar{r} \tag{2.18}$$

$$\begin{aligned} C_{Hpr} &= \frac{1}{2\pi}\int_0^1\int_0^{2\pi}\frac{1}{2}\sigma\frac{U^2}{(\Omega R)^2}C_d\cos\phi\sin\psi\ d\psi\ d\bar{r} \\ &= \frac{1}{4\pi}\sigma C_d\int_0^1\int_0^{2\pi}\frac{U^2}{(\Omega R)^2}\cos\phi\sin\psi\ d\psi\ d\bar{r} \end{aligned}$$

With the small ϕ assumption,

$$\begin{aligned} C_{Hpr} &= \frac{1}{4\pi}\sigma C_d\int_0^1\int_0^{2\pi}\frac{U_T^2}{(\Omega R)^2}\sin\psi\ d\psi\ d\bar{r} \\ &= \frac{1}{4\pi}\sigma C_d\int_0^1\int_0^{2\pi}(\mu^2\cos^2\alpha\sin^2\psi + \bar{r}^2 + 2\mu\cos\alpha\sin\psi\ \bar{r})\sin\psi\ d\psi\ d\bar{r} \\ &= \frac{1}{4\pi}\sigma C_d[\pi\mu\cos\alpha] \\ &= \frac{1}{4}\sigma C_d\ \mu\cos\alpha \end{aligned}$$

2.2.2 Induced Drag Component

The induced drag horizontal force coefficient can found similarly,

$$C_{Hind} = \frac{1}{2\pi}\int_0^1\int_0^{2\pi} dC_{Hind}\ d\psi\ d\bar{r} \tag{2.19}$$

$$C_{Hind} = \frac{1}{2\pi}\int_0^1\int_0^{2\pi}\frac{1}{2}\sigma\frac{U^2}{(\Omega R)^2}C_l\sin\phi\sin\psi\ d\psi\ d\bar{r}$$
$$= \frac{1}{4\pi}\sigma\int_0^1\int_0^{2\pi}\frac{U^2}{(\Omega R)^2}C_l\sin\phi\sin\psi\ d\psi\ d\bar{r}$$

With lift curve slope expansion and the small ϕ assumptions, we have

$$C_{Hind} = \frac{1}{4\pi}\sigma\int_0^1\int_0^{2\pi}\frac{U_T^2}{(\Omega R)^2}C_{l\alpha}(\theta+\phi)\ \phi\sin\psi\ d\psi\ d\bar{r}$$
$$= \frac{1}{4\pi}\sigma C_{l\alpha}\left(\int_0^1\int_0^{2\pi}\frac{U_T^2}{(\Omega R)^2}\theta\ \phi\sin\psi\ d\psi\ d\bar{r} + \int_0^1\int_0^{2\pi}\frac{U_T^2}{(\Omega R)^2}\phi^2\sin\psi\ d\psi\ d\bar{r}\right)$$

Substituting above equation with equation 2.10, we have

$$C_{Hind} = \frac{1}{4\pi}\sigma C_{l\alpha}\left(\int_0^1\int_0^{2\pi}\frac{U_T^2}{(\Omega R)^2}\ \theta\ \frac{U_P}{U_T}\sin\psi\ d\psi\ d\bar{r} + \int_0^1\int_0^{2\pi}\frac{U_T^2}{(\Omega R)^2}\ \frac{U_P^2}{U_T^2}\sin\psi\ d\psi\ d\bar{r}\right)$$
$$= \frac{1}{4\pi}\sigma C_{l\alpha}\left(\theta\int_0^1\int_0^{2\pi}\frac{U_T U_P}{(\Omega R)^2}\sin\psi\ d\psi\ d\bar{r} + \int_0^1\int_0^{2\pi}\frac{U_P^2}{(\Omega R)^2}\sin\psi\ d\psi\ d\bar{r}\right)$$

By equation 2.7 and equation 2.9, the equation would reduce to,

$$C_{Hind} = \frac{1}{4\pi}\sigma C_{l\alpha}\left(\theta\int_0^1\int_0^{2\pi}(\mu\cos\alpha\sin\psi+\bar{r})\lambda\sin\psi\ d\psi\ d\bar{r} + \int_0^1\int_0^{2\pi}\lambda^2\sin\psi\ d\psi\ d\bar{r}\right)$$
$$= \frac{1}{4\pi}\sigma C_{l\alpha}\left(\theta\ \pi\ \mu\lambda\cos\alpha + \ 0\right)$$
$$= \frac{1}{4}\sigma C_{l\alpha}\ \theta\ \mu\cos\alpha\ \lambda$$

The horizontal force coefficient can be given as,

$$C_H = C_{Hpr} - C_{Hind}$$
$$= \frac{1}{4}\sigma C_d\ \mu\cos\alpha - \frac{1}{4}\sigma C_{l\alpha}\ \theta\ \mu\cos\alpha\lambda$$
$$C_H = \frac{1}{4}\sigma\mu\cos\alpha\ (C_d - C_{l\alpha}\ \theta\lambda) \tag{2.20}$$

2.3 Torque

The total elemental torque of the rotor can be mathematically established as,

$$dQ = r(N_b dD\cos\phi - N_b dL\sin\phi)$$

Breaking them down as the profile and induced component.

$$dQ_{pr} = \frac{1}{2} N_b \rho U^2 C_d r dr \cos\phi$$
$$dQ_{ind} = \frac{1}{2} N_b \rho U^2 C_l r dr \sin\phi$$

The coefficient of torque can therefore be defined as,

$$dC_Q = \frac{dQ}{\rho A(\Omega R)^2 R} = dC_{Qpr} - dC_{Qind}$$

The Profile Torque is,

$$dC_{Qpr} = \frac{dQ_{pr}}{\rho A(\Omega R)^2 R} = \frac{1}{2}\sigma \frac{U^2}{(\Omega R)^2} C_d \frac{r}{R}\ d\bar{r}\cos\phi = \frac{1}{2}\sigma \frac{U^2}{(\Omega R)^2} C_d\ \bar{r}\ d\bar{r}\cos\phi \tag{2.21}$$

The Induced Torque is expanded as,

$$dC_{Qind} = \frac{dQ_{ind}}{\rho A(\Omega R)^2 R} = \frac{1}{2}\sigma \frac{U^2}{(\Omega R)^2} C_l \frac{r}{R}\ d\bar{r}\sin\phi = \frac{1}{2}\sigma \frac{U^2}{(\Omega R)^2} C_l\ \bar{r}\ d\bar{r}\sin\phi \tag{2.22}$$

Similarly to thrust and horizontal force the total torque coefficient can be obtained by integrating over the azimuth from 0 to 2π and over the non-denationalised radial distance from 0 to 1.

2.3.1 Profile Torque

The Profile torque coefficient is given as,

$$C_{Qpr} = \frac{1}{2\pi}\int_0^1 \int_0^{2\pi} dC_{Qpr}\ d\psi\ d\bar{r} \tag{2.23}$$

$$\begin{aligned} C_{Qpr} &= \frac{1}{2\pi}\int_0^1 \int_0^{2\pi} \frac{1}{2}\sigma \frac{U^2}{(\Omega R)^2} C_d\ \bar{r}\cos\phi\ d\psi\ d\bar{r} \\ &= \frac{1}{4\pi}\sigma C_d \int_0^1 \int_0^{2\pi} \frac{U^2}{(\Omega R)^2}\ \bar{r}\cos\phi\ d\psi\ d\bar{r} \end{aligned}$$

With the small ϕ assumption,

$$\begin{aligned} C_{Qpr} &= \frac{1}{4\pi}\sigma C_d \int_0^1 \int_0^{2\pi} \frac{U_T^2}{(\Omega R)^2}\ \bar{r}\ d\psi\ d\bar{r} \\ &= \frac{1}{4\pi}\sigma C_d \int_0^1 \int_0^{2\pi} (\mu^2 \cos^2\alpha \sin^2\psi + \bar{r}^2 + 2\mu\cos\alpha\sin\psi\ \bar{r})\ \bar{r}\ d\psi\ d\bar{r} \\ &= \frac{1}{4\pi}\sigma C_d \left[\frac{\pi}{2}(\mu^2\cos^2\alpha + 1)\right] \\ &= \frac{1}{8}\sigma C_d\ (\mu^2\cos^2\alpha + 1) \end{aligned}$$

2.3.2 Induced Torque

The induced torque coefficient is,

$$C_{Qind} = \frac{1}{2\pi}\int_0^1\int_0^{2\pi} dC_{Qind}\ d\psi\ d\bar{r} \tag{2.24}$$

$$\begin{aligned} C_{Qind} &= \frac{1}{2\pi}\int_0^1\int_0^{2\pi}\frac{1}{2}\sigma\frac{U^2}{(\Omega R)^2}C_l\ \bar{r}\sin\phi\ d\psi\ d\bar{r} \\ &= \frac{1}{4\pi}\sigma\int_0^1\int_0^{2\pi}\frac{U^2}{(\Omega R)^2}C_l\ \bar{r}\sin\phi\ d\psi\ d\bar{r} \end{aligned}$$

With lift curve slope expansion and the small ϕ assumptions, we have

$$\begin{aligned} C_{Qind} &= \frac{1}{4\pi}\sigma\int_0^1\int_0^{2\pi}\frac{U_T^2}{(\Omega R)^2}C_{l\alpha}(\theta+\phi)\ \bar{r}\phi\ d\psi\ d\bar{r} \\ &= \frac{1}{4\pi}\sigma\ C_{l\alpha}\left(\int_0^1\int_0^{2\pi}\frac{U_T^2}{(\Omega R)^2}\theta\ \phi\ \bar{r}\ d\psi\ d\bar{r} + \int_0^1\int_0^{2\pi}\frac{U_T^2}{(\Omega R)^2}\phi^2\ \bar{r}\ d\psi\ d\bar{r}\right) \end{aligned}$$

Substituting above equation with equation 2.10, we have

$$\begin{aligned} C_{Qind} &= \frac{1}{4\pi}\sigma\ C_{l\alpha}\left(\int_0^1\int_0^{2\pi}\frac{U_T^2}{(\Omega R)^2}\theta\ \frac{U_P}{U_T}\ \bar{r}\ d\psi\ d\bar{r} + \int_0^1\int_0^{2\pi}\frac{U_T^2}{(\Omega R)^2}\frac{U_P^2}{U_T^2}\ \bar{r}\ d\psi\ d\bar{r}\right) \\ &= \frac{1}{4\pi}\sigma\ C_{l\alpha}\left(\int_0^1\int_0^{2\pi}\frac{U_T U_P}{(\Omega R)^2}\theta\ \bar{r}\ d\psi\ d\bar{r} + \int_0^1\int_0^{2\pi}\frac{U_P^2}{(\Omega R)^2}\ \bar{r}\ d\psi\ d\bar{r}\right) \end{aligned}$$

By equation 2.7 and equation 2.9, the equation would reduce to,

$$\begin{aligned} C_{Qind} &= \frac{1}{4\pi}\sigma\ C_{l\alpha}\left(\theta\int_0^1\int_0^{2\pi}(\mu\cos\alpha\sin\psi+\bar{r})\lambda\ \bar{r}\ d\psi\ d\bar{r} + \int_0^1\int_0^{2\pi}\lambda^2\ \bar{r}\ d\psi\ d\bar{r}\right) \\ &= \frac{1}{4\pi}\sigma\ C_{l\alpha}\left(\theta\frac{2}{3}\pi\lambda + \pi\lambda^2\right) \\ &= \frac{1}{12}\sigma\ C_{l\alpha}\ \lambda\ (2\theta+3\lambda) \end{aligned}$$

The coefficient of torque can be established as,

$$\begin{aligned} C_Q &= C_{Qpr} - C_{Qind} \\ &= \frac{1}{8}\sigma C_d\ (\mu^2\cos^2\alpha+1) - \frac{1}{12}\sigma R\ C_{l\alpha}\lambda\ (2\theta+3\lambda) \\ C_Q &= \frac{1}{4}\sigma\left[C_d\frac{\mu^2\cos^2\alpha+1}{2} - C_{l\alpha}\frac{2\theta\lambda+3\lambda^2}{3}\right] \end{aligned} \tag{2.25}$$

In steady motion, the torque must be set to zero and hence the state of rotation is given by the equation,

$$3\ C_d(\mu^2\cos^2\alpha+1) - 2\ C_{l\alpha}(2\theta\lambda+3\lambda^2) = 0 \tag{2.26}$$

2.4 Summary

On the basis of the above three coefficients, the aerodynamic characteristics of an auto-rotating rotor is defined by four essential parameters [14]:-

θ - pitch angle of blades

σ - solidity ratio

$C_{l\alpha}$ - lift curve slope

C_d - coefficient of drag

Substituting the above known or assumed values, a system of equations with four unknowns are developed. Summarizing from equation 2.3, 2.15, 2.20 and 2.26,

$$\begin{aligned}
\lambda &= \mu \sin\alpha - \frac{C_T}{2\sqrt{(\mu\cos\alpha)^2 + \lambda^2}} \\
C_T &= \frac{1}{12}\sigma\left[C_{l\alpha}\ (3\theta\mu^2\cos^2\alpha + 2\theta + 3\lambda) + 3C_d\lambda\right] \\
C_H &= \frac{1}{4}\sigma\mu\cos\alpha\ (C_d - C_{l\alpha}\ \theta\lambda) \\
&3\ C_d(\mu^2\cos^2\alpha + 1) - 2\ C_{l\alpha}(2\theta\lambda + 3\lambda^2) = 0
\end{aligned} \tag{2.27}$$

The four unknowns being μ, λ, C_T and C_H. The above coefficients are non-dimensionalized with respect to the tip speed, where in it is required to non-dimensionalize with the free stream velocity V_∞ for standardization. Hence,

$$C'_T = \frac{T}{\rho A V_\infty^2}$$

$$C_T = \frac{T}{\rho A(\Omega R)^2}\frac{V_\infty^2}{V_\infty^2} = \frac{T}{\rho A V_\infty^2}\frac{V_\infty^2}{(\Omega R)^2} = \frac{C'_T}{\mu^2}$$

Therefore,

$$C'_T = \frac{C_T}{\mu^2} \qquad C'_H = \frac{C_H}{\mu^2} \tag{2.28}$$

The rotor lift and drag coefficients can be therefore calculated as,

$$C'_L = C'_T\cos\alpha - C'_H\sin\alpha \qquad C'_D = C'_T\sin\alpha + C'_H\cos\alpha \tag{2.29}$$

The above set of equations are solved on a MATLAB solver, similar to as described by the code in APPENDIX A.

Glauert [14], develops a theory, on the assumption that angles of incidence of the blade elements are small, and only first order harmonics of periodic terms need to be retained in the equations. Also, Glauert ignores all periodic terms while deriving the inflow angle ϕ. The work here mainly differs in a way that it includes the higher order periodic terms, also ϕ includes the periodic terms. But it considers no flapping, where as Glauert does. Glauert's [14] original work, only shows the performance parameters varying from 0° to 45°. But since this thesis is focused on the range from 0° to 90°, Glauret's model is run for the range of 0° to 90°. Glauert's model is solved on MATLAB as well with the code as described in APPENDIX B. Both model's solvers on MATLAB blow up near 0°, hence the calculations are initiated from 2°. The following aerodynamic parameters are assumed for the analysis:

$\theta = 2°$

$\sigma = 0.2$

$C_{l\alpha} = 6$

$C_d = 0.006$

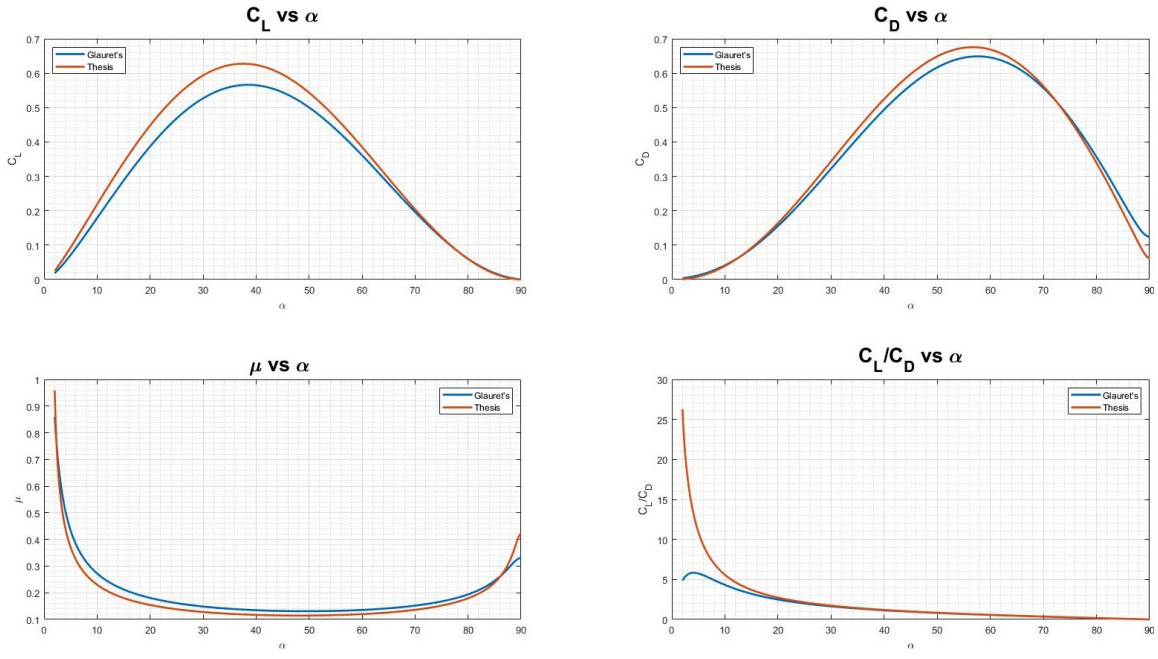

Figure 9. Glauret's Model Compared with Thesis Model

It can be clearly visualized that the thesis' model works with very close match with Glauert's model. The slight overshoots are due to the considerations of higher order periodic terms of velocities. Similarly in the section below, a model including linear twist is developed, and results are again compared with Glauert's model.

2.5 Linearly Twisted Rotor

All rotors, contain some span-wise twist, in different forms and magnitudes. They allow to avoid blade stalling and also to gain a little uniform distribution of lift over the span. Different applications call for different optimizations for twist. For simple models, ideal twist and linear twist are two very common. Ideal twist tries to maintain an uniform inflow, but it becomes physically unrealizable near the root due its hyperbolic nature. But they are often used with hub and root cut out. Linear twist models are also a good approximation of the ideal twist. They prove to be reasonable the same towards the tip [5]. With a linear twist, the localised blade pitch can be given as,

$$\theta(\bar{r}) = \theta_0 + \bar{r}\theta_{tw} \qquad or \qquad \theta(\bar{r}) = \theta_{75} + (\bar{r} - 0.75)\theta_{tw}$$

where, θ_0 is the pitch measured near the root of the blade, θ_{75} is measured at radial distance 75% of the radius, and θ_{tw} represents the blade twist rate per radius of the rotor (degrees per rotor radius) [5]. In this analysis the θ_{75} form is used, as practically it is easier to measure.

2.5.1 Thrust Coefficient

As from the previous Section 2.1, the lift component of thrust coefficient can be integrated as,

$$C_{TL} = \frac{1}{4\pi}\sigma C_{l\alpha}\left(\int_0^1\int_0^{2\pi}(\theta_{75} + (\bar{r} - 0.75)\theta_{tw})(\mu^2\cos^2\alpha\sin^2\psi + \bar{r}^2 + 2\mu\cos\alpha\sin\psi\ \bar{r})\right.$$
$$\left. d\psi\ d\bar{r} + \int_0^1\int_0^{2\pi}(\mu\cos\alpha\sin\psi + \bar{r})\ \lambda\ d\psi\ d\bar{r}\right)$$

$$C_{TL} = \frac{1}{4\pi}\sigma C_{l\alpha}\left[\frac{\pi}{12}(8\theta_{75} + 12\mu^2\theta_{75}\cos^2\alpha - 3\mu^2\theta_{tw}\cos^2\alpha) + \pi\lambda\right]$$
$$= \frac{1}{48}\sigma C_{l\alpha}\ \left(8\ \theta_{75} + 12\ \theta_{75}\mu^2\cos^2\alpha - 3\ \theta_{tw}\mu^2\cos^2\alpha + 12\lambda\right)$$

The drag component isn't affected by the twist since it has no coefficient of lift. Therefore the thrust coefficient including linear twist can be given as,

$$C_T = C_{TL} + C_{TD}$$
$$= \frac{1}{48}\sigma C_{l\alpha}\ \left(8\ \theta_{75} + 12\ \theta_{75}\mu^2\cos^2\alpha - 3\ \theta_{tw}\mu^2\cos^2\alpha + 12\lambda\right) + \frac{1}{4}\sigma C_d\lambda$$

$$C_T = \frac{1}{48}\sigma\left[C_{l\alpha}\left(8\ \theta_{75} + 12\ \theta_{75}\mu^2\cos^2\alpha - 3\ \theta_{tw}\mu^2\cos^2\alpha + 12\lambda\right) + 12C_d\lambda\right] \quad (2.30)$$

2.5.2 Horizontal Force Coefficient

As from the previous Section 2.2, the profile component of H-force does not the change. But the Induced component, can be integrated as,

$$C_{Hind} = \frac{1}{4\pi}\sigma C_{l\alpha}\left(\int_0^1\int_0^{2\pi}(\theta_{75} + (\bar{r} - 0.75)\theta_{tw})(\mu\cos\alpha\sin\psi + \bar{r})\lambda\sin\psi\ d\psi\ d\bar{r}\right.$$
$$\left. + \int_0^1\int_0^{2\pi}\lambda^2\sin\psi\ d\psi\ d\bar{r}\right)$$

$$C_{Hind} = \frac{1}{4\pi}\sigma C_{l\alpha}\left[\frac{\pi}{4}(4\theta_{75} - \theta_{tw})\ \mu\lambda\cos\alpha + \ 0\right]$$
$$= \frac{1}{16}\sigma C_{l\alpha}\ (4\theta_{75} - \theta_{tw})\ \mu\cos\alpha\ \lambda$$

The horizontal force coefficient including linear twist can be given as,

$$C_H = C_{Hpr} - C_{Hind}$$
$$= \frac{1}{4}\sigma C_d\ \mu\cos\alpha - \frac{1}{16}\sigma C_{l\alpha}\ (4\theta_{75} - \theta_{tw})\ \mu\cos\alpha\ \lambda$$

$$C_H = \frac{1}{16}\sigma\mu\cos\alpha\ (4C_d - 4\theta_{75}C_{l\alpha}\lambda + \theta_{tw}C_{l\alpha}\lambda) \quad (2.31)$$

2.5.3 Torque Coefficient

Similarly, from Section 2.3, the profile component of torque does not the change. But the Induced component, can be integrated as,

$$C_{Qind} = \frac{1}{4\pi}\sigma\ C_{l\alpha}\Bigg(\theta\int_0^1\int_0^{2\pi}(\theta_{75}+(\bar{r}-0.75)\theta_{tw})(\mu\cos\alpha\sin\psi+\bar{r})\lambda\ \bar{r}\ d\psi\ d\bar{r} + \int_0^1\int_0^{2\pi}\lambda^2\ \bar{r}\ d\psi\ d\bar{r}\Bigg)$$

$$\begin{aligned} C_{Qind} &= \frac{1}{4\pi}\sigma\ C_{l\alpha}\left(\frac{2\pi}{3}\theta_{75}\lambda+\pi\lambda^2\right) \\ &= \frac{1}{12}\sigma\ C_{l\alpha}\ \lambda\ (2\theta_{75}+3\lambda) \end{aligned}$$

The coefficient of torque including linear twist can be given as,

$$\begin{aligned} C_Q &= C_{Qpr} - C_{Qind} \\ &= \frac{1}{8}\sigma C_d\ (\mu^2\cos^2\alpha+1) - \frac{1}{12}\sigma R\ C_{l\alpha}\lambda\ (2\theta_{75}+3\lambda) \\ C_Q &= \frac{1}{4}\sigma\left[C_d\frac{\mu^2\cos^2\alpha+1}{2} - C_{l\alpha}\frac{2\theta_{75}\lambda+3\lambda^2}{3}\right] \end{aligned} \tag{2.32}$$

For autorotation,

$$3\ C_d(\mu^2\cos^2\alpha+1) - 2\ C_{l\alpha}(2\theta_{75}\lambda+3\lambda^2) = 0 \tag{2.33}$$

2.5.4 Summary of Equations using Linear Twist

Based on linear twist model, the equations 2.3, 2.30, 2.31 and 2.33 give,

$$\begin{aligned} &\lambda = \mu\sin\alpha - \frac{C_T}{2\sqrt{(\mu\cos\alpha)^2+\lambda^2}} \\ &C_T = \frac{1}{48}\sigma\left[C_{l\alpha}\left(8\ \theta_{75}+12\ \theta_{75}\mu^2\cos^2\alpha-3\ \theta_{tw}\mu^2\cos^2\alpha+12\lambda\right)+12C_d\lambda\right] \\ &C_H = \frac{1}{16}\sigma\mu\cos\alpha\ (4C_d-4\theta_{75}C_{l\alpha}\lambda+\theta_{tw}C_{l\alpha}\lambda) \\ &3\ C_d(\mu^2\cos^2\alpha+1) - 2\ C_{l\alpha}(2\theta_{75}\lambda+3\lambda^2) = 0 \end{aligned} \tag{2.34}$$

Similar to what is done in the previous section, using the same aerodynamic parameters the model with linear twist of $-5°$ is compared. The code to solve the system of equations is described in APPENDIX A.

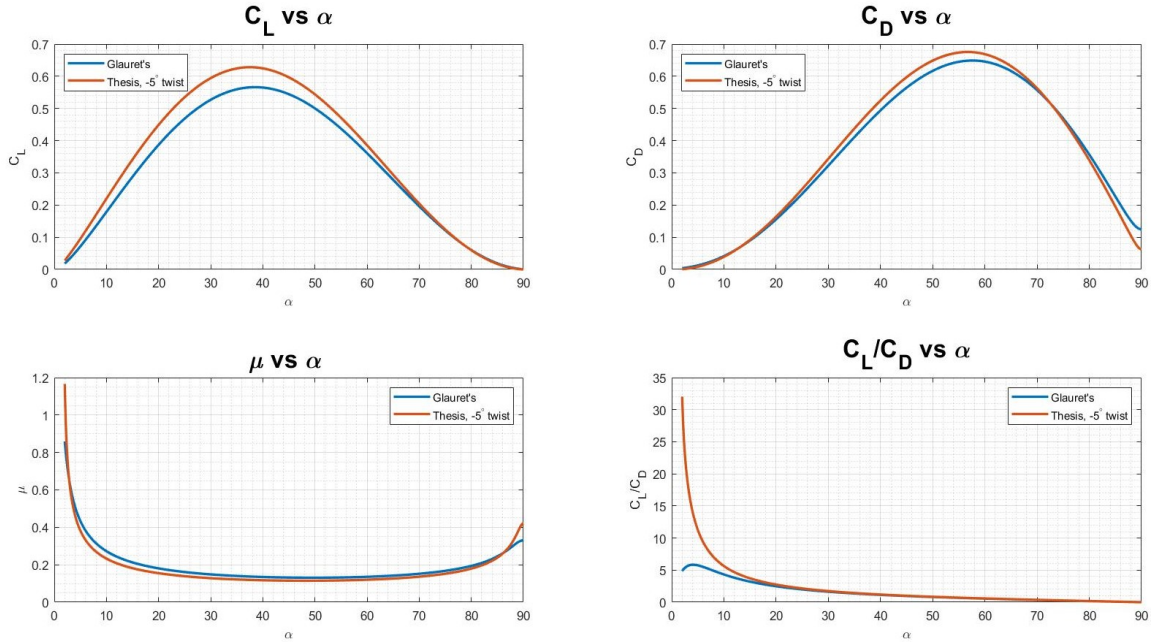

Figure 10. Glauret's Model Compared with Thesis Model with Twist

2.6 Additional Analysis

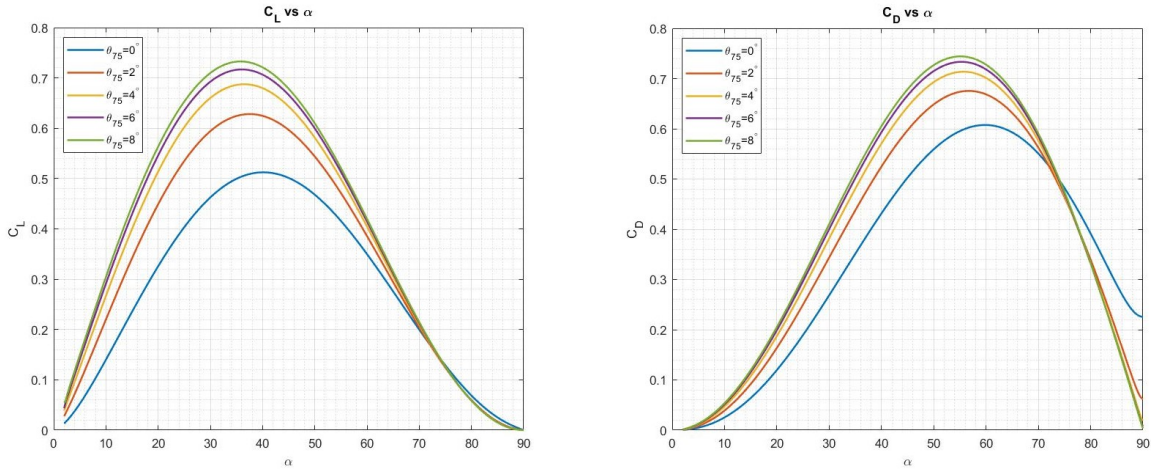

Figure 11. Coefficient of Lift and Drag for Varying Pitch

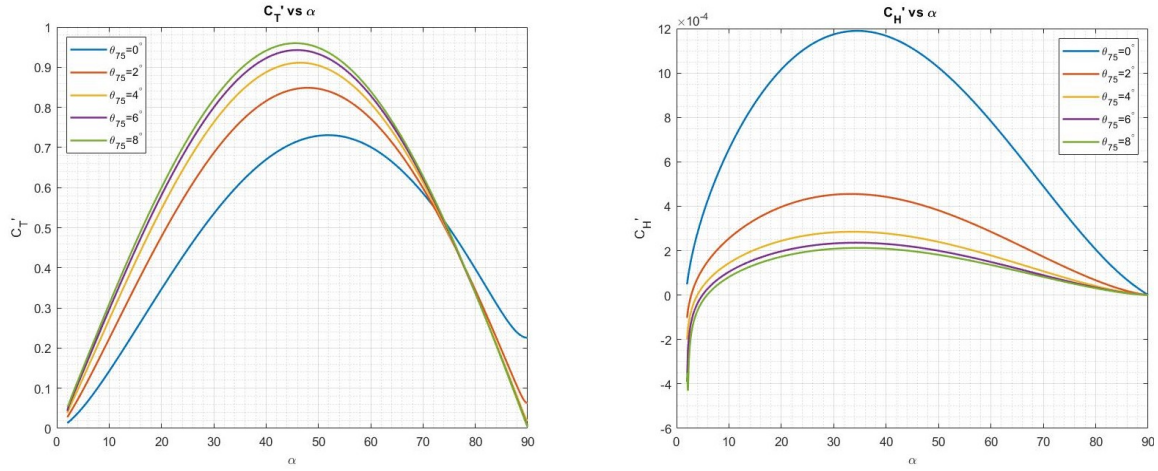

Figure 12. Thrust Coefficient and Horizontal Force for Varying Pitch

To observe the effect of varying the pitch, θ_{75} is varied as 0,2,4,6 and 8 degrees. Using the same aerodynamic parameters, the lift and drag coefficient variation over α is shown in Figure 11. Similarly the variation of pitch angle is plotted for thrust coefficient and horizontal force coefficient in Figure 12. It is being observed that as pitch increases, the coefficients of lift, drag and thrust increase. The horizontal force coefficient decreases with increasing pitch angle.

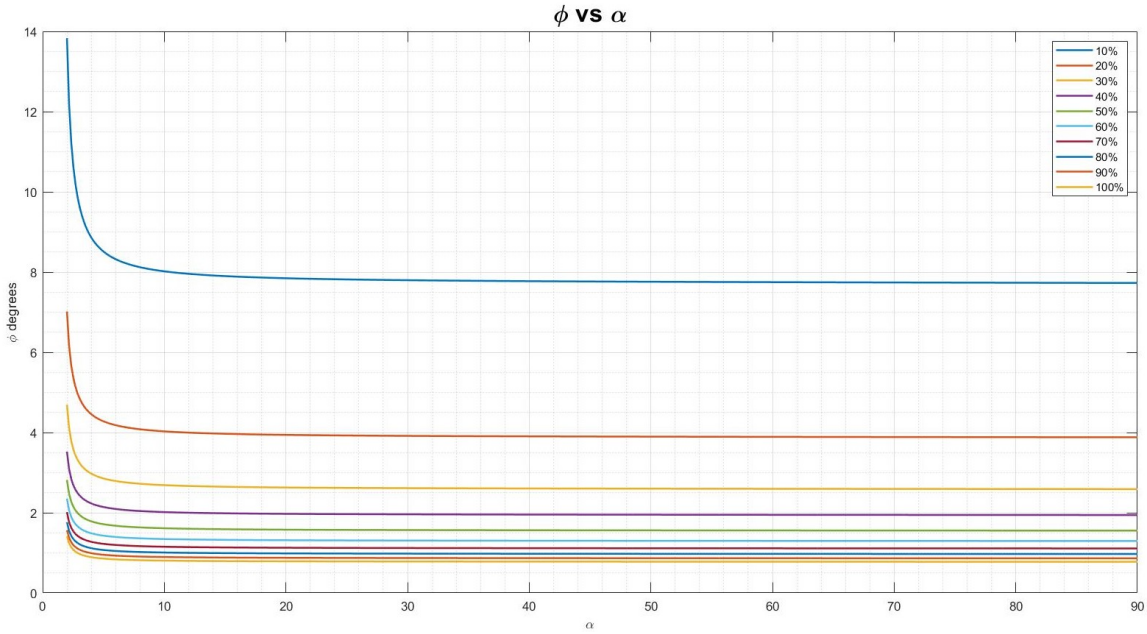

Figure 13. Verification of Small Angle Assumption for ϕ

In the beginning it was assumed that ϕ was a small angle. To verify this assumption, ϕ was calculated and plotted for 10 radial elements.

$$\phi = tan^{-1}\frac{U_P}{U_T} = tan^{-1}\frac{U_P/\omega R}{U_T \omega R} = tan^{-1}\frac{\lambda}{\mu \cos\alpha \sin\psi + \bar{r}}$$

Ignoring the periodic term for ease of solving, hence:

$$\phi = tan^{-1}\frac{\lambda}{\bar{r}}$$

It can observed from Figure 13 that 80% of the blade encounters an induced inflow angle less than 5°, hence we can conclude that the small angle assumption is an good assumption.

In the subsequent chapters, the model developed here will be used to simulate results using the aerodynamic parameters of experimented rotors.

Chapter 3

WIND TUNNEL

There have been various research reports available which provide information about rotor being supplied with torque. But rarely any data is found to correlate the state of autorotation at various angles of the rotor plane. To envision the condition of autorotation experimentally various rotors are simulated in the wind tunnel. An auto-rotating rotor can posses the capability to sustain flight just on the basis of aerodynamic forces generated due to flow passing through it. In this scenario the net torque supplied to or extracted from the rotor is zero. To maintain an analogy of the condition, the rotor was introduced into the wind tunnel such that it can free-wheel. The rotor plane angle was then varied from being parallel to the flow, to being perpendicular to the flow while carrying out force measurements. The total angular sweep was 90°. For this particular research study the custom built Low Speed Wind Tunnel at Arizona State University was used.

3.1 Low Speed Wind Tunnel

The ASU Flow Visualization Wind Tunnel is an Open Circuit type configuration with a 0.5m long and 0.5m diameter octagonal test section. A maximum wind speed of 30 m/s can be achieved with an empty test section. The four major duct components of the wind tunnel are the contraction, the test section, the diffuser and the fan housing. The contraction contour is defined by a fifth order polynomial with a contraction ratio of 25:1. The test section walls diverge from inlet to outlet to reduce buoyancy effects due to boundary layer thickness. The diffuser is a linearly expanding octagonal section which decelerates the flow without stalling. A transition area at the end of the diffuser changes the cross section from octagonal to circular to accommodate the fan. The diffuser's total-included shallow divergence angle 4° allows to eliminate diffusion

Figure 14. ASU Wind Tunnel

effects in the tunnel. The fan and motor is a separate unit attached to the tunnel. It has its own stand to isolate vibrations from the tunnel. The fan is connected by 10 HP motor which has a maximum rotational speed of 57.3 Hz. The fan speed is controlled by a Variable Frequency Drive (VFD). The open circuit tunnel draws fresh air from the surrounding environment which is filtered and straightened out by a an inlet fairing attached around the entrance to the tunnel, four honeycomb matrix cell sheets and four tensioned turbulence-reducing screens. These allow to eliminate axial velocity variation in the flow. The wind speed inside the tunnel is determined using static pressure sensing in the test section followed by post processing of raw data. The NI Labview data acquisition code reports a real-time value for the wind velocity in the tunnel. The system is equipped with mainly two electronic instrumentation components, a solid state differential pressure transducers and a three component sting Force/Moment balance. Figure 14 above shows a picture of the ASU wind tunnel. The force balance data acquisition system is interfaced with a Aerolab software platform. This software reads raw balance data, filters it with a root mean squared averaging function and passes it through data reduction matrix to derive forces. The balance module in the DAQ tool, reports raw and tared component loads in either SI or BG

unit systems. The acquired data is filtered and processed for any derivations at a specified data rate. All readings taken for this research were configured for a data rate of 10Hz.

A Force balance by Aerolab (schematic shown below in figure 15) with 3/8-inch diameter cylindrical "sting" and a parallelogram base is installed in the test section in the wind tunnel. The strain gauge allows to measure two forces and one moment simultaneously. The default configuration has been used which provides signals for Normal Force, Axial Force, and Pitching Moment. The maximum specified load limits is 111.2 N for Normal Force, 44.5 for Axial Force and 5.65 N-m for Pitching Moment. The manufacturer suggests to allow 45 minutes for warm-up to permit optimal stabilization of the signals [20]. It must me noted that the weight of the mounted model, affect all three component readings as a function of angle of attack. Hence, it is imperative to perform a zero wind speed pitch sweep to gauge gravitational corrections for each component over the outlined pitch angle range. With the current setup, the force balance can traverse an angle of $+30°$ and $-20°$.

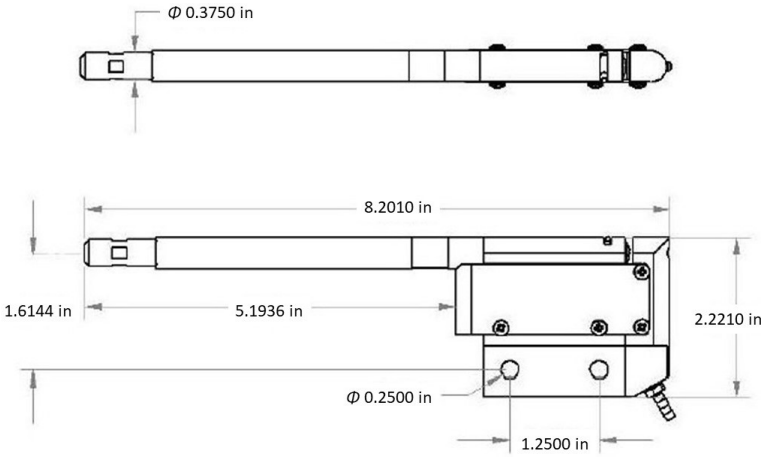

Figure 15. "Pistol Grip" Sting Balance [20]

3.2 Mount and Model Development

To mount a test model on the sting, it must be equipped with a cylindrical socket like the one shown in Figure below. The dimensions are such that Length A must be 0.900 inches (22.86mm), Diameter B 0.375 inches (9.525mm), Diameter C 0.625 inches (15.875mm), Length D must not exceed 5.0 inches (127mm), and Length E is the distance between the end of the socket and the center of the set screw where, E must be 0.50 inches (12.7mm). A set screw of #8 or smaller should be used to constraint the machined aluminum mount.

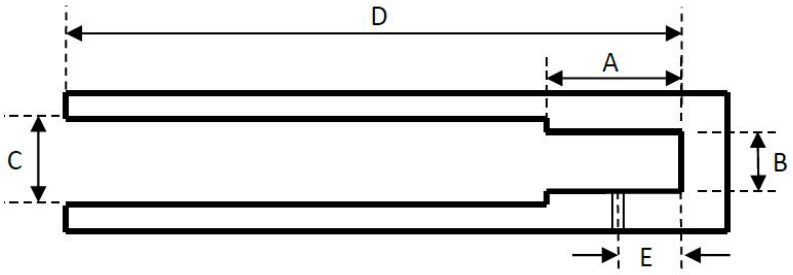

Figure 16. Custom Model Mounting Socket [20]

With regards to the above dimensions a generalised aluminium machined mount was developed, which could be used to fit wings, propellers, aircraft models, etc. The mount had been designed and manufactured by ASU's SEMTE Student Machine Shop. The Figure 17 below (not to scale) shows the mount.

Now, to fit a rotor on to force balance, a secondary customized mount was designed. This mount was an intermediate attachment between the rotor and the generalised aluminium mount. This secondary mount would assemble over the aluminium mount and the rotor would then fit over it. As per our experimentation objectives, we would like to traverse from zero degrees to ninety degrees, but this was limited to the force balance as it allowed only a 50 degree pitch. Hence, it was envisioned to build the

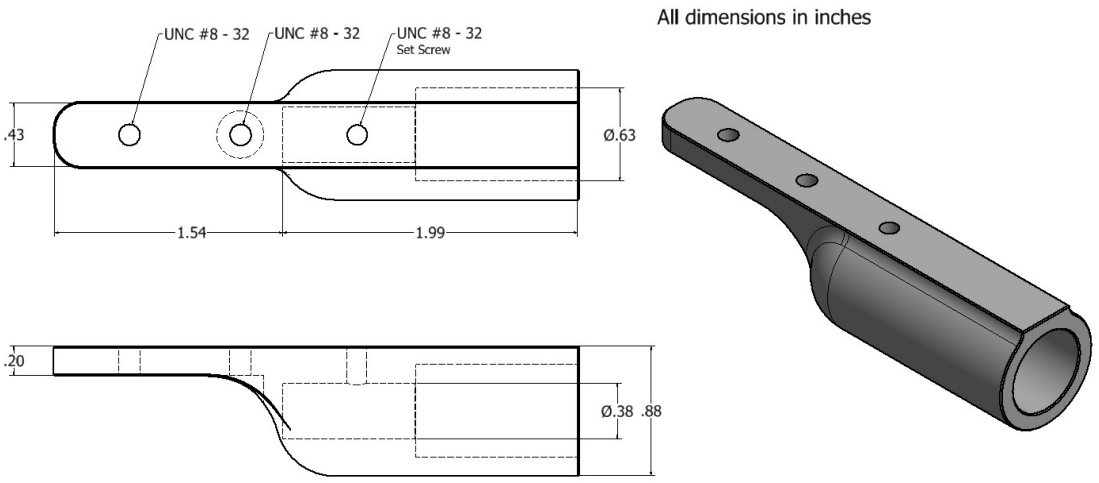

Figure 17. Generalized Force Balance Mount

secondary mounts in such a way that it would posses a relative angle between the rotor axis and force balance axis.

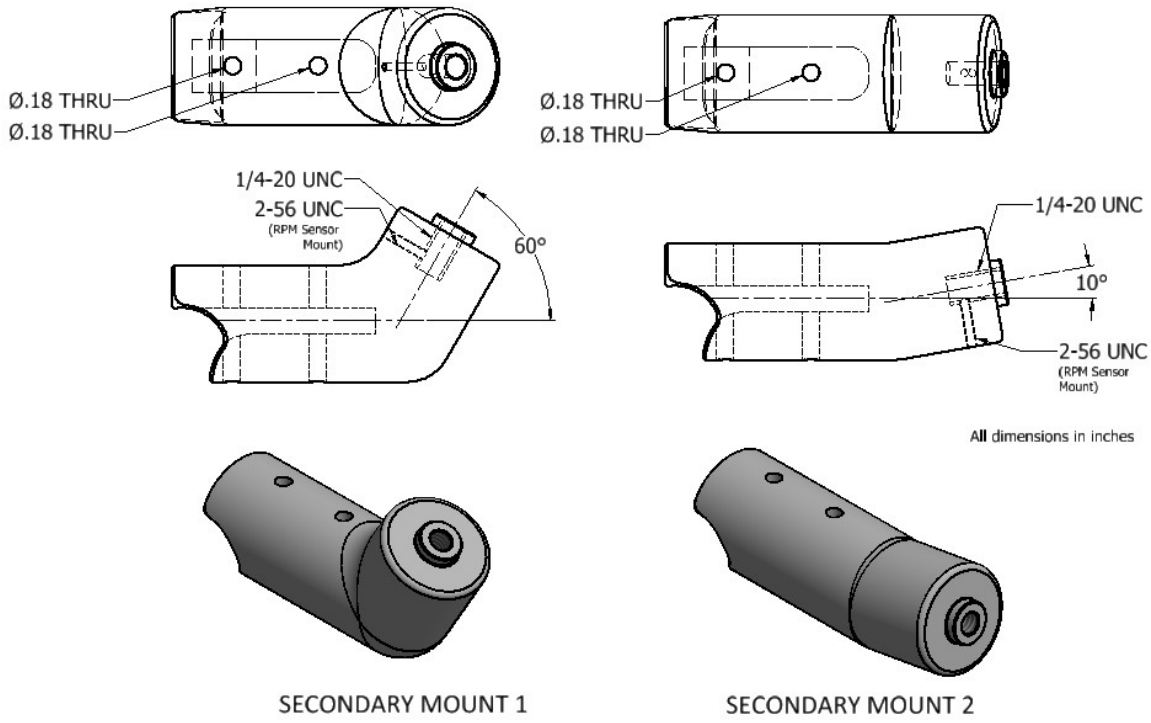

Figure 18. Propeller Sleeve Mounts

The first mount was designed at angle of 60° and the other at 10° relative to the horizontal axis. Therefore, the first mount allowed the rotor to encounter the flow from being at zero degrees ($90° - 60° - 30°$) to fifty degrees ($90° - 60° + 20°$) relative to the wind flow and the second mount supported the rotor to encounter the flow from fifty degrees ($90° - 10° - 30°$) to hundred degrees ($90° - 10° + 20°$), where the fifty degree angle was a cross over point. It must be noted that the upper limit for the force balance pitch was $+30°$ and the lower limit was $-20°$. The two mounts have been shown in Figure 18 (not to scale). These mounts, were manufactured by Fused Deposition Modelling (FDM). The parts were printed by a Stratasys Mojo machine, where the material used was ABS plastic. A layer thickness of 0.17mm with an infill density of 15% was used. The support material was removed by bath of sodium hydroxide (NaOH).

Further to select rotors, it was needed that autorotation can be experimented with a more optimized rotor functioning for example like an airborne wind turbine. Hence, it would be great to design our own customized rotor for this purpose. But, this would require machining of nylon, aluminium like materials and/or developing molds for fibreglass on a small scale to constrain the rotor diameter size to the wind tunnel test section. This could have been time consuming and expensive, therefore for simplicity standard UAV propellers which are easily available in the market were selected. Brands like Master Airscrew, Graupner, APC and Xoar were used for trial runs. The final results are all from propellers of Master Airscrew.

To prepare the selected model for testing it was needed to fit a bearing in the propeller so that it can free-wheel on its axis of rotation. To obtain slightly higher magnitude of forces, larger diameter propellers were selected. All test propellers had a hub diameter of greater than 20mm and a hub thickness greater than 14mm. With regards these geometric dimensions, Shielded Ball Bearings were selected to allow the propeller to freely rotate along its axis.

Bearing Specifications:

Model: R4 ZZ

Brand: PGN International

Material: 100% Chrome Steel

Protection: Metal Shield on both sides

Greased / Lubricated: Yes

Bore (Inner) Diameter: 1/4”

Outer Diameter: 5/8”

Width (Thickness): 0.196”

Supported RPM: 38,000

Load Rating: 1489 N

Static Load Rating: 618 N

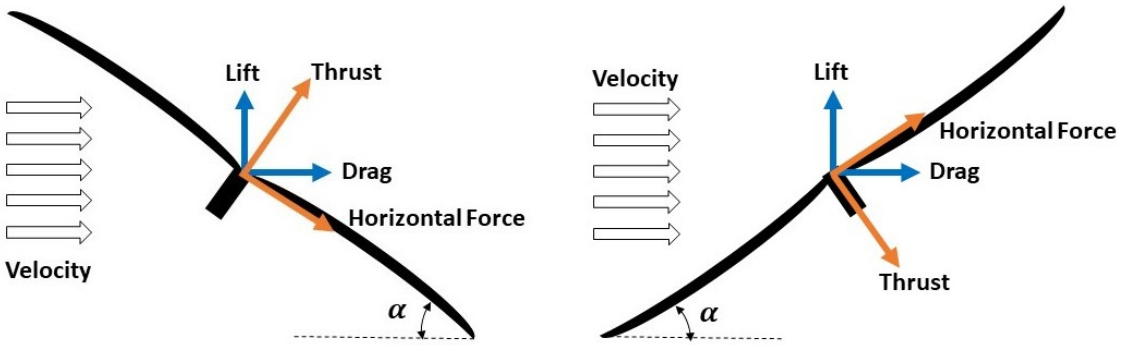

(a). General (b). Wind Tunnel

Figure 19. Autorotation

These bearings were inserted with an interference fit into the propeller which had been earlier milled to create a housing for the bearing. Also, the propeller center hole must be enlarged to 0.42 inches before the bearing insertion to later allow clear movement of the constraining bolt. It must be carefully noted that the bearings were fit on the front (top) facing side of the propeller. This was intentionally done as the force balance can only pitch with its mounting edge pointing to the oncoming flow. In the most common sense to envision autorotation we must orient the rotor as shown in Figure 19 (a). But since the propeller cannot be pitched in this way on the wind tunnel, the configuration was mirrored about the horizontal axis, with the shaft flipped to the other side as in Figure 19 (b).

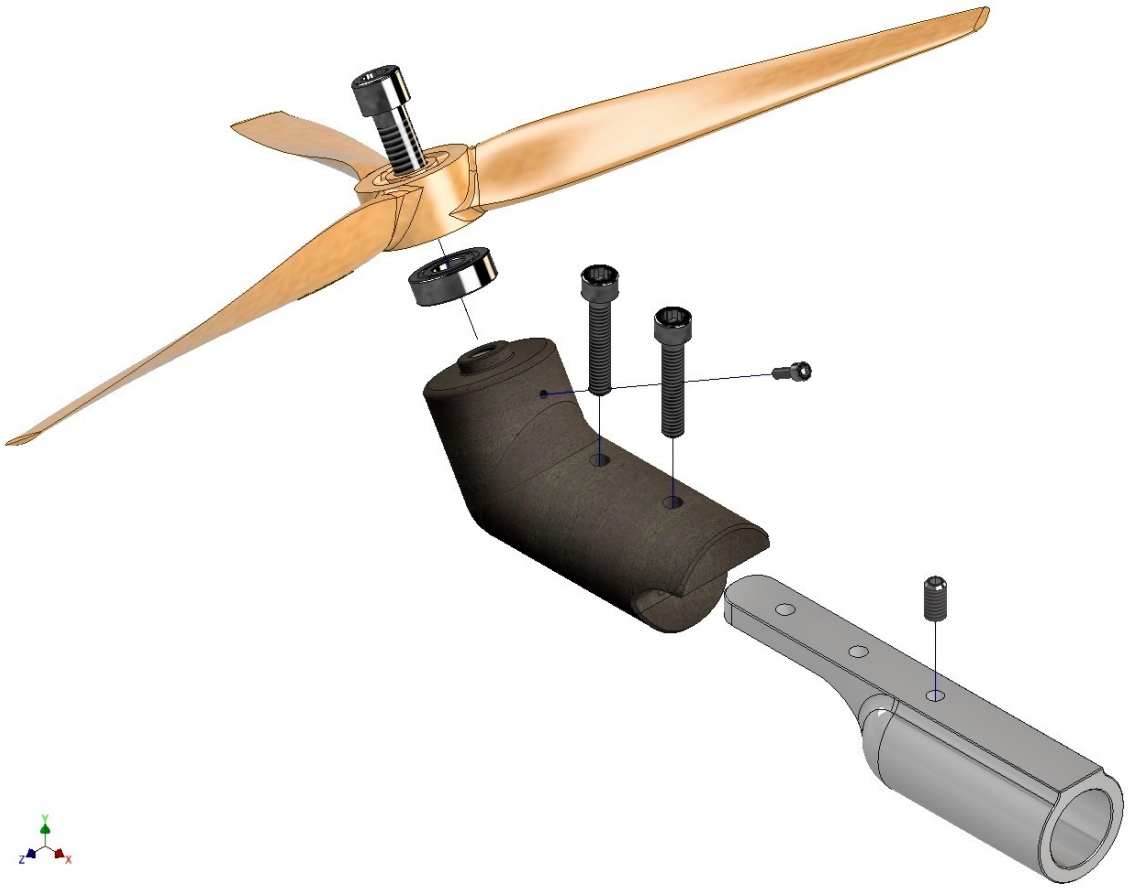

Figure 20. Exploded View of Propeller Mount Assembly

To assemble the setup for testing, the 3-D printed sleeve was first fixed on to aluminium mount by two 8-32 UNC socket headed screws. Now, to attach the propeller to the mount, a machined 1/4-20 UNC socket headed bolt was needed. The bolt head was machined to a diameter of 0.38 inches, so that the head would just rest on the bearing's inner race (diameter of 0.4 "), allowing no contact point between the rotating propeller and the static sleeve. For all free wheeling rotational frequency measurement an Infrared Reflective sensor by Honeywell (HOA0149-001) was utilized. The sensor consists of an infrared emitting diode and an NPN silicon phototransistor encased side-by-side on converging optical axes in a black thermoplastic housing.The sensor was fixed on the sleeve by a 2-64 UNC screw. Lastly this entire assembly was delicately mounted onto the force balance pistol, and slowly tightened by the a 8-32

set screw. It must be taken care not apply excessive force on the Force Balance as it might change the calibration. Figure 20 shows the exploded view of the entire assembly.

3.3 Experimental Procedure

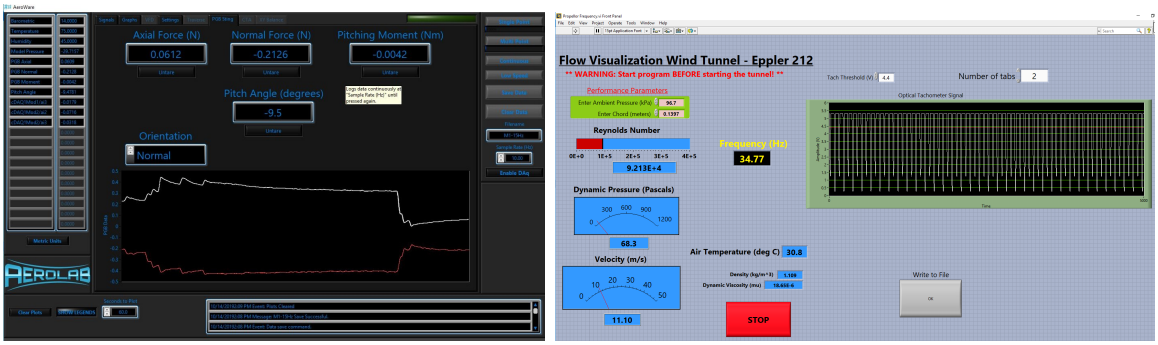

(a). Aeroware (b). NI Labview

Figure 21. Software Tools used for Data Acquisition

Conducting the experiment consisted of setting up the experimental hardware, data acquisition (DAQ) system and calibration of measuring instruments. This thesis does not include the methodology for setting up the DAQ systems nor the calibration of instruments. An already established and calibrated test setup was used. The data was recorded through two data acquisition software, Aeroware by Aerolab for the force measurements, and NI Labview for the Velocity and RPM measurements. Figure 21 (a) shows the screenshot of the Aerolab tool and Figure 21 (b) shows the NI Labview User Interface. This section will first discuss the initial developments with the experimentation. Then lastly will outline the procedural steps to carryout measurements and recording of data.

3.3.1 Initial Runs

After successful assembly mountings on to the wind tunnel, various rotors were tested to determine the lift, drag, thrust and horizontal force. During several test runs it was noticed there were discontinuities between in the curves of forces at the

overlapping region of two mounts. Ideally the magnitudes of resolved forces should equate, for the same angles. Figure 22 shows the sudden change in forces at a 50° angle.

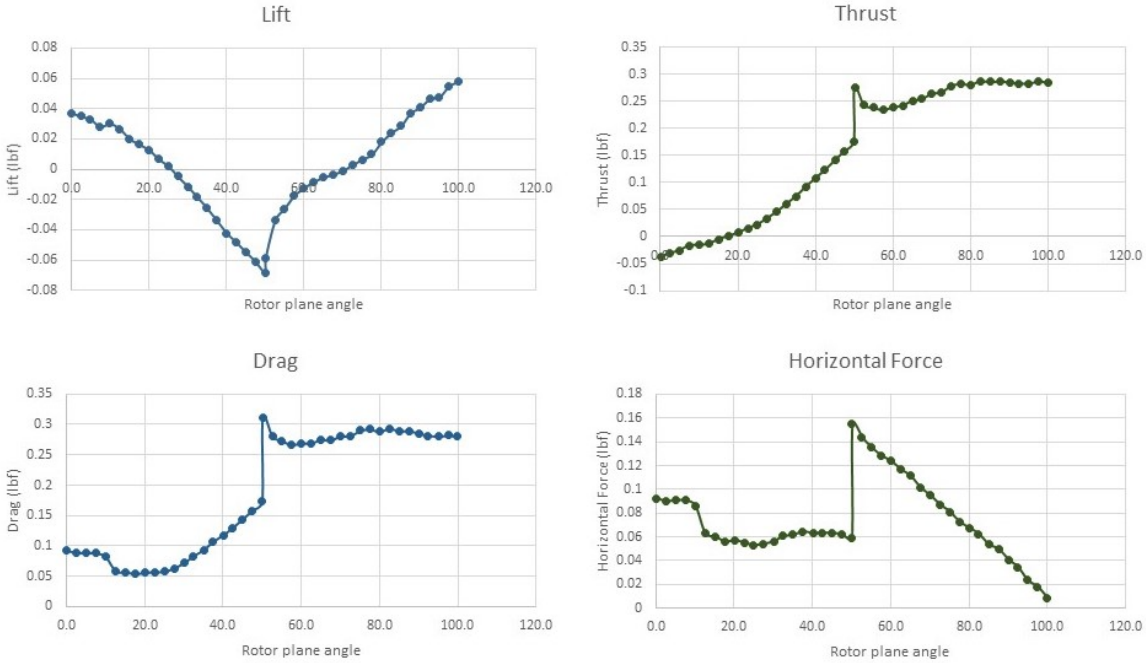

Figure 22. Discontinuities in Force Curves

The reason of the discontinuity was broken down to two major causes:-

- The magnitudes of forces are very small, the profile drag on the individual mounts can be significantly varying.
- At the extreme pitch angle ends of the force balance, the strain gauge is not being consistent.

To investigate the first idea, the mounts were placed in the wind tunnel without any rotors. The profile axial and normal forces only for the mounts were measured. Later these forces were subtracted from the axial and normal forces measured with the propeller. These effective forces were used to calculate Lift, Drag, etc. Figure 28 shows the comparison forces for a Master Airscrew 12×7 propeller for accounting

and not accounting the profile drag for a velocity of 10.8 m/s. Similarly, Figure 24 shows the same for a wind tunnel air velocity of 15 m/s. The 15Hz and 20Hz denote the fan speed of the tunnel.

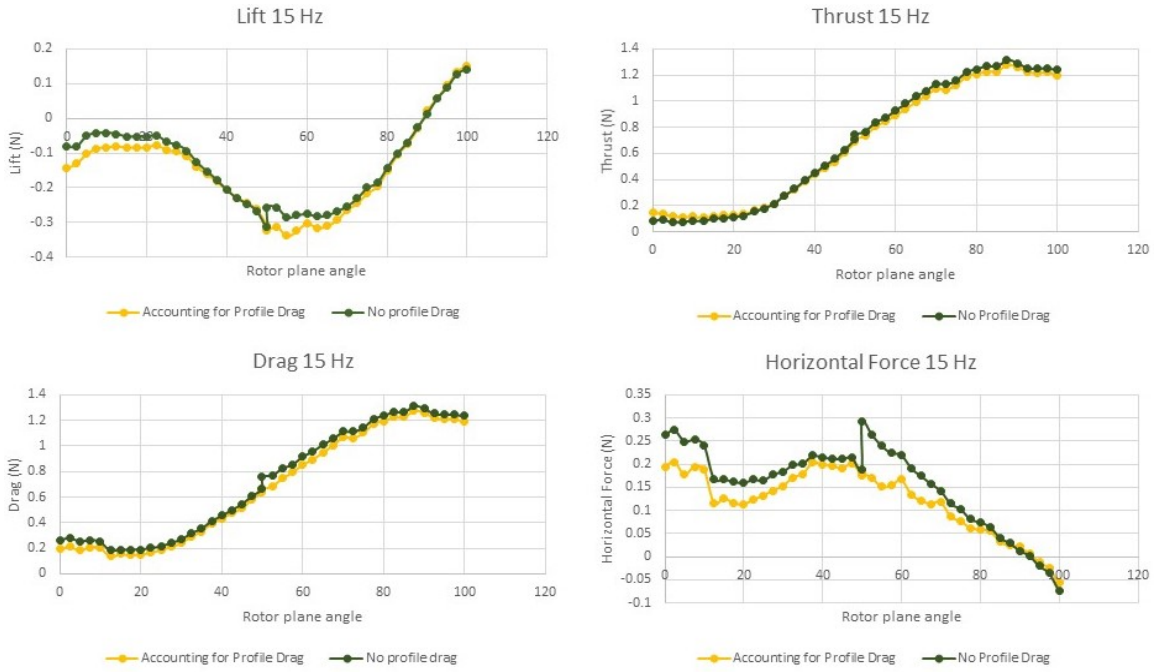

Figure 23. Effect of Profile Drag on Force Plots - 15Hz Fan Speed

It can be clearly noted that the profile drag on the mounts was a major influence for the discontinuities seen earlier. Accounting for these losses greatly improve the curves. The profile drag on mounts can be also seen to loose its effects on the force calculations with higher velocities as the loads on the rotor start to increase in magnitude, except for the case of horizontal force.

Even though subtracting the profile drag forces reduced the discontinuities largely, there a few disruptions left which could be seen on the horizontal force plot particularly. These were especially seen using other propellers of XOAR, Graupner, etc. (plots not shown). With this, the second cause of discontinuity was explored. Since the two mounts were forced to operate at the extremities of the force balance pitch angle, three mounts were now designed and manufactured which could traverse in an interior range

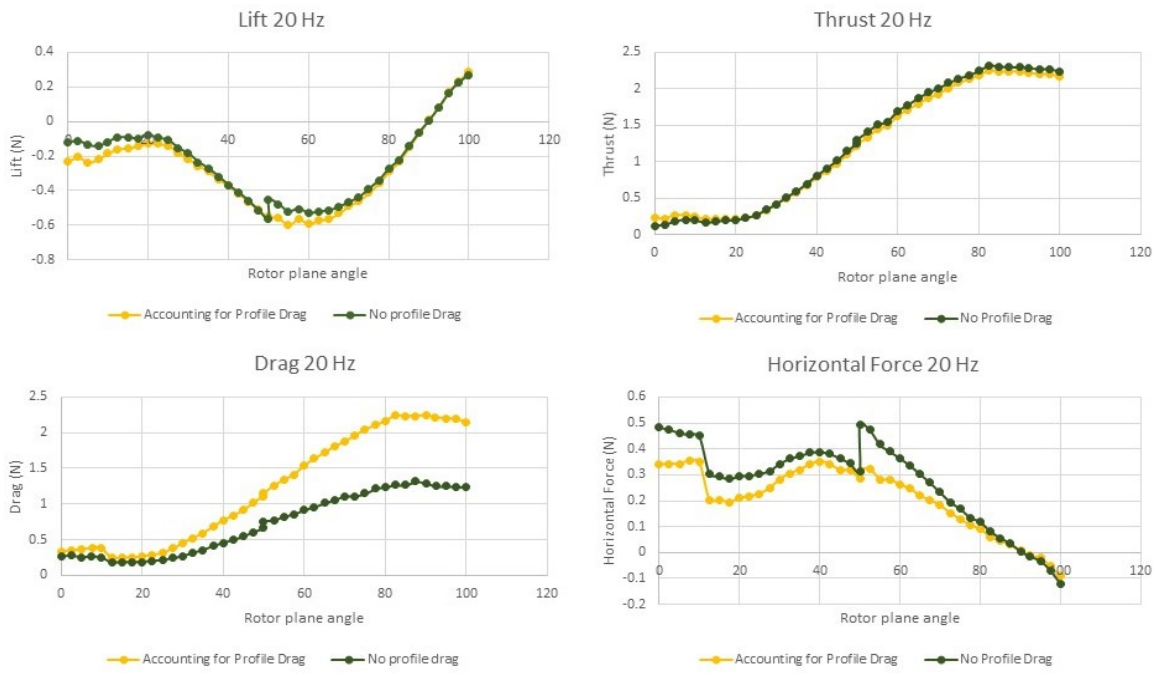

Figure 24. Effect of Profile Drag on Force Plots - 20Hz Fan Speed

of angles. Similar to the parts shown in Figure 18, three mounts having a relative angle of 5°, 40°, 75° were developed. This angle is the angle measured between the rotor axis and horizontal. The purpose of this was to primarily work with multiple overlapping points. The new mounts allowed the rotor encounter the flow in the following range:

- Mount 1 (75°) - 0° $(90° - 75° - 15°)$ to 35° $(90° - 75° + 20°)$
- Mount 2 (40°) - 22.5° $(90° - 40° - 27.5°)$ to 70°$(90° - 40° + 20°)$
- Mount 3 (5°) - 57.5° $(90° - 5° - 27.5°)$ to 105° $(90° - 5° + 20°)$

The force balance pitched between 15° and $-20°$ for the first mount, while it pitched between 27.5° and $-20°$ for the second and third mount. Carrying out the experiments at in interval of 2.5°, six overlapping points were obtained in two regions:

- First overlapping region - 22.5°, 25°, 27.5°, 30°, 32.5°, 35°.
- Second overlapping region - 57.5°, 60°, 62.5°, 65°, 67.5°, 70°.

Using these three mounts, the experiment was performed with the same 12×7 Master Airscrew propeller. Figure 25 and Figure 26 show the various plots for forces for a velocity of 10.8 m/s, and 15 m/s respectively. These plots account for the profile drags on the respective mounts.

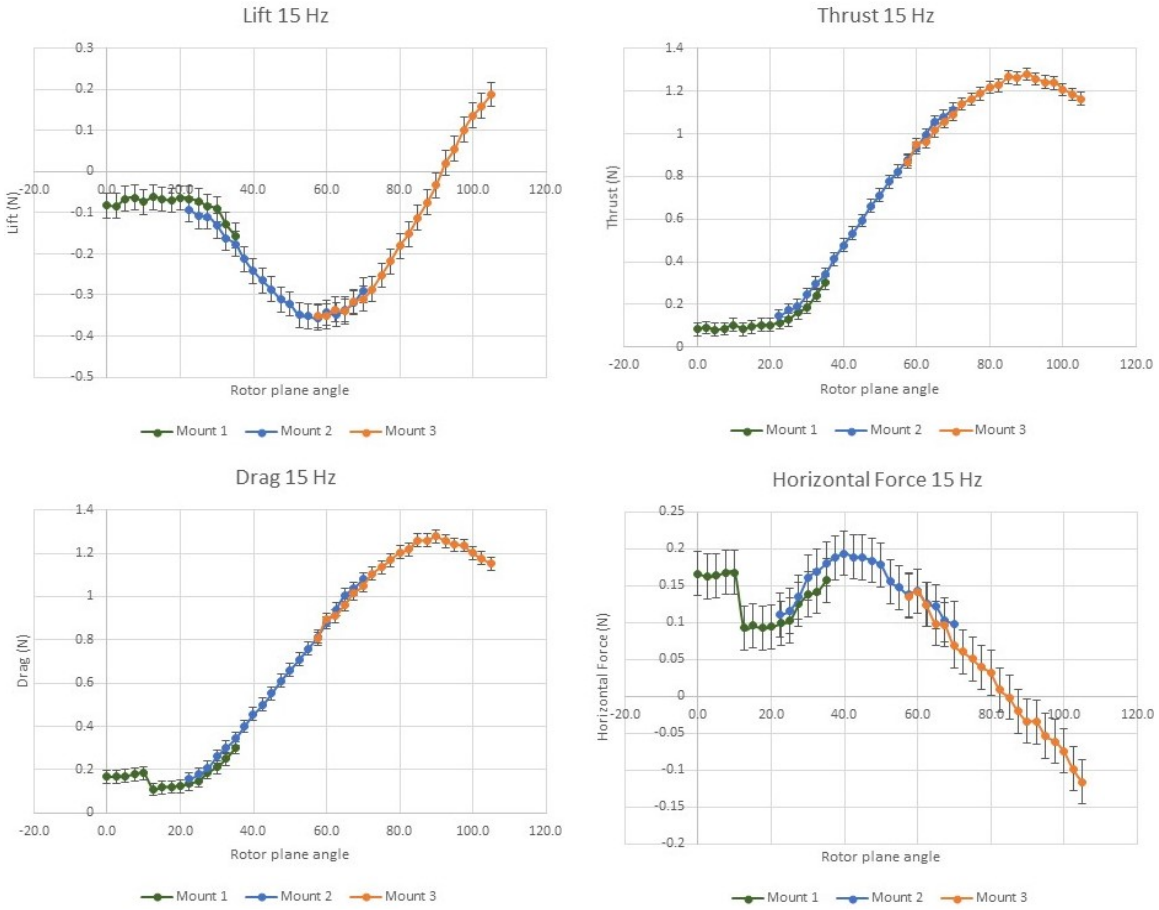

Figure 25. Force Mounts with Multiple Overlapping Points - 15Hz Fan Speed

On both the figures, it can be seen that there are variations at multiple points in both the overlap regions. The variations are observed to be greater in the case of lower wind speed. Whereas at the higher wind speeds, the magnitudes of forces increase, and therefore the magnitude of discontinuities also decrease. Therefore we can rule out the idea that at the extremities of the force balance pitch angles, there are variations in readings.

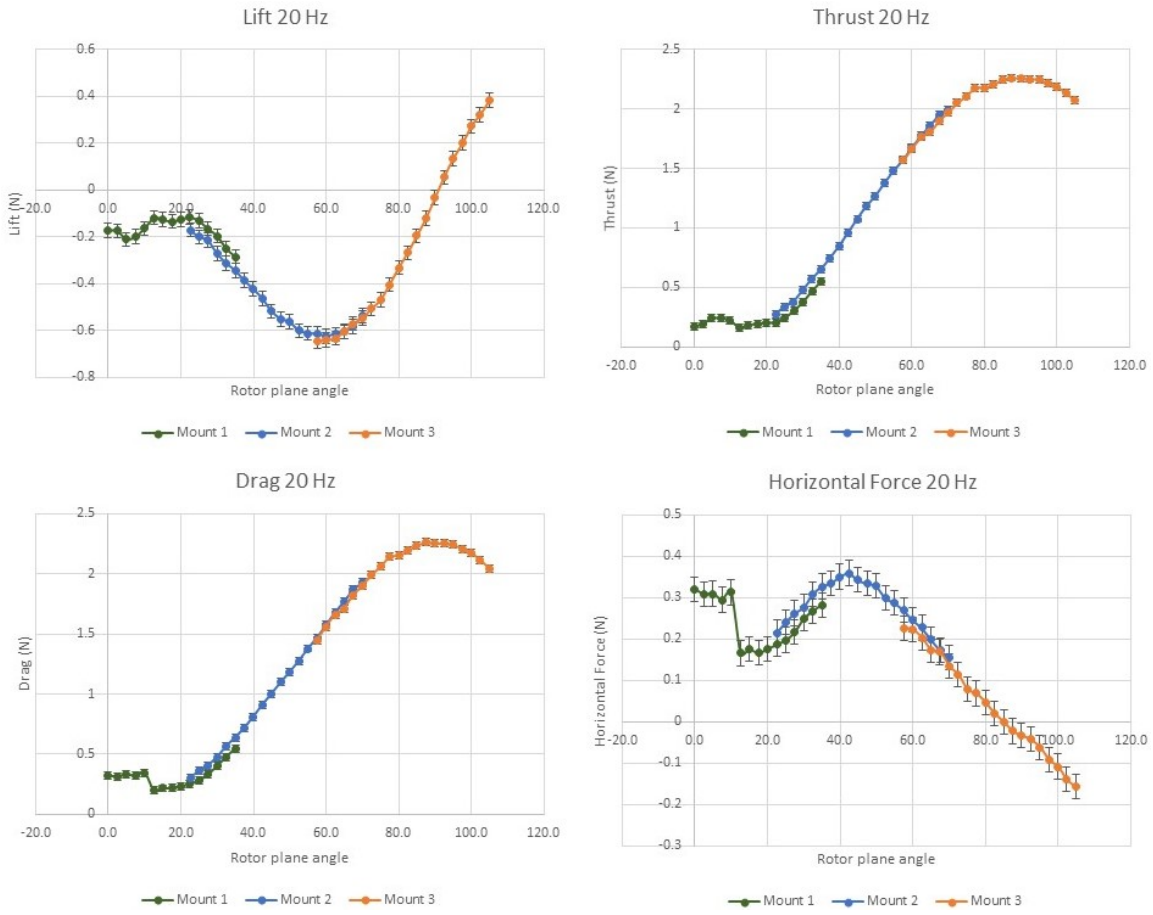

Figure 26. Force Mounts with Multiple Overlapping Points - 20Hz Fan Speed

The Master Airscrew propeller was run in the test rig several times with two mounts and three mounts. After the subtraction of profile drag forces, it was observed that there is a repeatability of the force magnitudes for the particular angle of rotor, with occasional variations been seen with the discontinuities. On Figure 25 and Figure 26 error bars are plotted with a variation of 0.03 N. Error bars graphical represent the variability of data and are used to indicate the error or uncertainty in a measurement. They give a general idea of how precise a measurement is, or conversely, how far from the reported value the true value might be. With these experimental results, it can be visualized that most of the readings lie within the range of 0.03 N error. It was therefore concluded that the slight variation in readings seen for the same rotor angle from different mounts are associated with inherent calibration of the strain gauge.

The magnitudes of forces are very small, hence the overall variation is considered to be acceptable within $1/30^{th}$ of a newton.

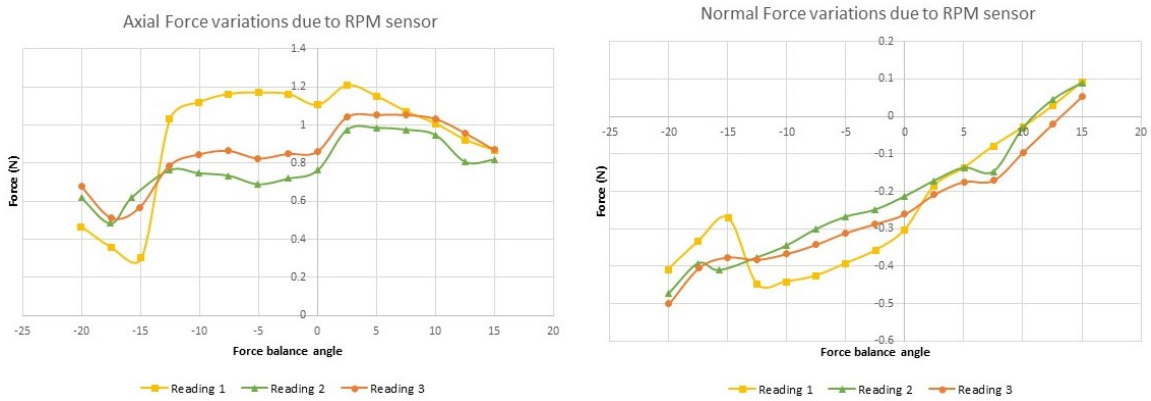

Figure 27. Force Variations due to RPM Sensor - Master Airscrew 12×8

Lastly, large variations in force magnitudes were observed when the RPM sensor is mounted on the 3D printed sleeves. This was mainly due to wire exerting a gravitation pull on the force balance due to hanging. Figure 27 shows the variations for the same Mount 1, same wind speed of 15m/s, and same propeller. It is therefore highly suggested to take the angular velocity measurements separate from for the force measurements.

3.3.2 Procedure

Having discussed the issues encountered with the experimental setup and having established the origins of various errors in measurement, this sub-section will enlist a detailed step by step procedure to conduct the experiment with minimum errors. All final tests very conducted with 3 mounts, with two regions of overlapping points. The average of two readings from the overlapping regions were used to evaluate Lift, Drag, Thrust and Horizontal Force.

1. The first step comprised of assembling the 3-D printed Sleeve Mount 1 (75°) over the aluminium mount. Note that at this stage there was no propeller. The assembled setup was then fixed onto the force balance.

2. The angle changing knob is turned to physically set the force balance angle at zero degrees.
3. Ensuring that the wind tunnel fan is switched off, all forces, angles and moments were tared.
4. The knob was then turned clockwise until the force balance angle was $+15^\circ$ read by the Aerolab software.
5. The data for this angle is recorded by clicking on the single point tab on the aerolab software.
6. The above step was repeated, traversing from $+15^\circ$ to -20° in intervals as required. An interval of 2.5° was used for this thesis. Note - there is no wind velocity at this stage, and will be referred as *Mount Gravitational*.
7. The data was saved from the Aerolab Software.
8. The force balance was traversed back to $+15^\circ$ angle. Ensure that the Lab View application is running to take note of the wind velocities. Now, the wind tunnel was switched on to a motor fan speed of 15 Hz.
9. Steps 5,6 and 7 were repeated with at this wind speed.
10. Steps 8 and 9 were reiterated for the fan motor speed now set to 20Hz. These data points will referred as *Mount Velocity*.
11. The exact same procedure was rerun using Mount 2 (40°) and Mount 3 (5°) following steps from 1 to 10. But, now the force balance must traverse from $+27.5^\circ$ to -20°.
12. At this time the assembled mount was carefully removed from the force balance. Then the propeller was fixed onto the mount assembly, and put back on the force balance sting as described at the end of Section 3.2 and in Figure 20.
13. Steps 2-11 were repeated with propeller mounted on. For future references, the "no wind" weight readings will be called *Gravitational Data* and the readings with the wind will be referred as *Propeller Data*.

14. Carefully dismount the propeller assembly from the force balance. Now, attach the RPM sensor delicately on the 3-D printed sleeve Mount 1, and constrain it to the mount with its screw. Put back the assembly on to the force balance. Ensure to manage the RPM sensor wires carefully to the DAQ hardware so that there is no interference during the sting movement.
15. Ensure the sting angle is tared at 0°. Turn the knob and traverse to +15°.
16. Run the motor at 15Hz, and record the data at each angle at an interval of 2.5° from the NI Labview Application. Traverse from +15° to −20° for Mount 1. This step would be recording the wind velocity in the tunnel, dynamic pressure and the RPM of the rotating propeller.
17. Repeat step 16 with the tunnel running at 20Hz fan speed.
18. Repeat steps 14 - 17, for Mount 2 and 3. Ensure to traverse between +27.5° to −20° for these mounts.
19. Compile all data for the three mounts, and save.

The angle nomenclature has been explained in Figure below. The rotor plane angle was established as:

$$\alpha = \frac{\pi}{2} - \gamma - \delta$$

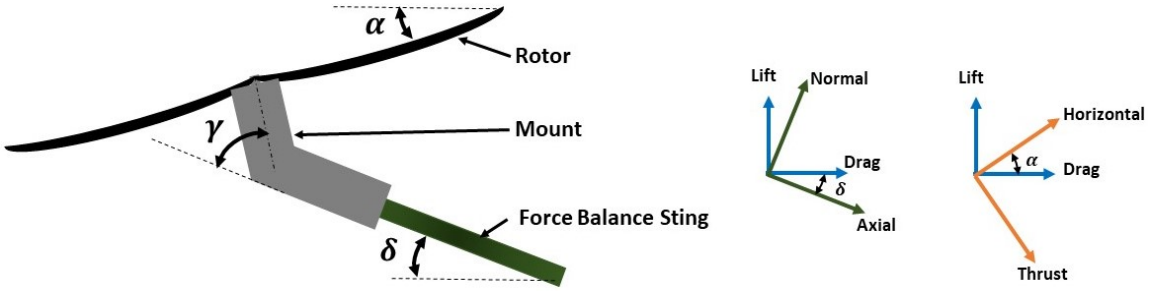

Figure 28. Diagrammatic Representation of Various Angles

The following set of equations were used to established to evaluate Lift, Drag, Thrust and Horizontal Force. All forces were calculated for the entire range of angles.

Axial Mount = Axial Mount Gravitation - Axial Mount Velocity

Normal Mount = Normal Mount Gravitation - Normal Mount Velocity

Axial Force (A) = Axial Propeller - Axial Gravitation - Axial Mount

Normal Force (A) = Normal Propeller - Normal Gravitation - Normal Mount

$$Lift(L) = N\cos\delta - A\sin\delta$$
$$Drag(D) = N\sin\delta + A\cos\delta \tag{3.1}$$

$$Thrust(T) = D\sin\alpha - L\cos\alpha$$
$$Horz(H) = D\cos\alpha + L\sin\alpha \tag{3.2}$$

The Thrust and Horizontal Force can also be directly calculated from the Axial and Normal Force as,

$$T = A\cos\gamma - N\sin\gamma$$
$$H = A\sin\gamma + N\cos\gamma$$

The final experimentation was run on five different propellers, all from Master Airscrew. Using the procedural steps of this chapter, the results are compiled and discussed in the following chapter.

Chapter 4

RESULTS AND DISCUSSION

To develop the results of the analytical model, we need to input specific aerodynamic parameters as mentioned in Chapter 2. These aerodynamic parameters are specific to a rotor, and hence we need to select particular rotors to compute the various coefficients of lift, drag, etc. For the purpose of the thesis, five propellers were selected from Master Airscrew. Three propellers were 2-bladed, and two were 3-bladed. All propellers were at $12in$ diameter, with varying pitch and made of fibre-glass composite. The 2-bladed propellers were specified as, 12×6, 12×7, and 12×8. Similarly the 3-bladed propellers were specified as, 12×6 and 12×8.

4.1 Defining Aerodynamic Constants

Solidity ratio plays an important role to estimate the potential of rotor to develop thrust. To determine the solidity ratio of the rotors, manual measurement was carried out using a vernier caliper. Each rotor, was divided into 12 sections, of $0.5in$. The chord length at each station was measured and used to compute the elemental blade area. The measurement at the first station was approximated to the value of second, as measurement at the blade root is difficult. The sum of all elemental areas, denoted the total blade area. The solidity ratio can be defined as,

$$\sigma = \frac{\text{Blade area}}{\text{Disk area}} = \frac{N_b \int_0^R c \; dr}{\pi R^2}$$

Table 1, shows the approximate evaluation of solidity ratio of each propeller.

Similarly, defining the blade pitch at 75% of each blade. Standard propellers are denoted with nomenclature as such 12×7, where 12 is the diameter of the rotor, and 7 is the geometric pitch. Geometric pitch is the distance a propeller should advance in one revolution with no slippage. Geometric pitch can roughly be related to the

Radial Distance	**Chord length (inch)**				
r (inch)	**2 - Blade 12x6**	**2 - Blade 12x7**	**2 - Blade 12x8**	**3 - Blade 12x6**	**3 - Blade 12x8**
0.5	0.811	0.877	0.671	0.733	0.733
1	0.811	0.877	0.671	0.733	0.733
1.5	0.872	0.909	0.95	0.751	0.853
2	0.931	0.956	1.06	0.801	0.925
2.5	0.974	0.984	1.011	0.859	0.933
3	1.019	1.005	1.044	0.863	0.944
3.5	1.034	1.019	1.074	0.876	0.923
4	0.999	0.987	1.102	0.854	0.882
4.5	0.918	0.894	0.945	0.811	0.865
5	0.818	0.775	0.832	0.754	0.785
5.5	0.717	0.683	0.729	0.686	0.704
6	0.627	0.598	0.637	0.599	0.625
Blade Area ($\sum c.dr$)	5.2655	5.2820	5.3630	4.6600	4.9525
# of blades	2	2	2	3	3
Disk Area (πR^2)	113.0973	113.0973	113.0973	113.0973	113.0973
Solidity	0.0931	0.0934	0.0948	0.1236	0.1314

Table 1. Solidity of Rotors

blade pitch angle at 3/4 radial distance as, $Geometric\ Pitch = 2\pi R\ \theta_{75}$. Therefore, the equation can be rearranged such that,

$$\theta_{75} = tan^{-1}\ \frac{\text{Geometric Pitch}}{2\pi R}$$

Table 2 shows, the calculated pitch angle at 75% radial distance.

Assuming the remaining aerodynamic coefficients as,

$\theta_{tw} = -5^{\circ}$

$C_{l\alpha} = 5$

$C_d = 0.02$

	2 - Blade 12x6	2 - Blade 12x7	2 - Blade 12x8	3 - Blade 12x6	3 - Blade 12x8
Geometric Pitch (inch)	6	7	8	6	8
Radius (inch)	6	6	6	6	6
$\boldsymbol{\theta_{75}}$	9.0431°	10.5189°	11.9808°	9.0431°	11.9808°

Table 2. Pitch Angle at 75% Radial Distance

Using all of the above constants for calculation, the aerodynamic characteristics are computed below, for all five rotors.

4.2 Analytical Results

4.2.1 2 Blade

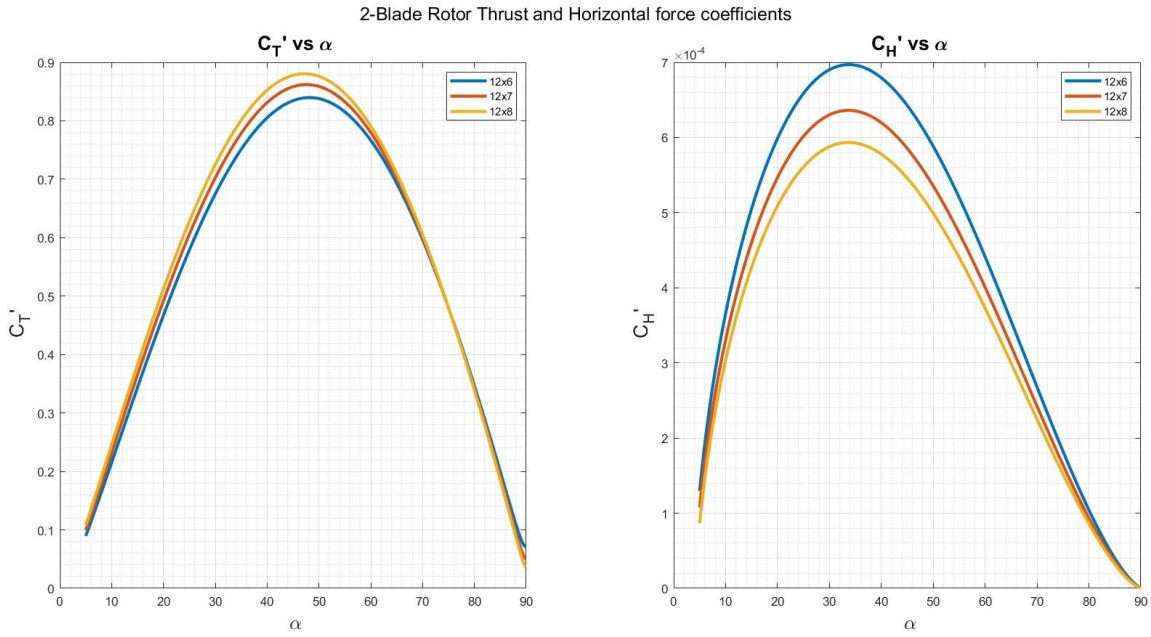

Figure 29. Analytical 2 Blade Coefficient of Thrust and Horizontal Force

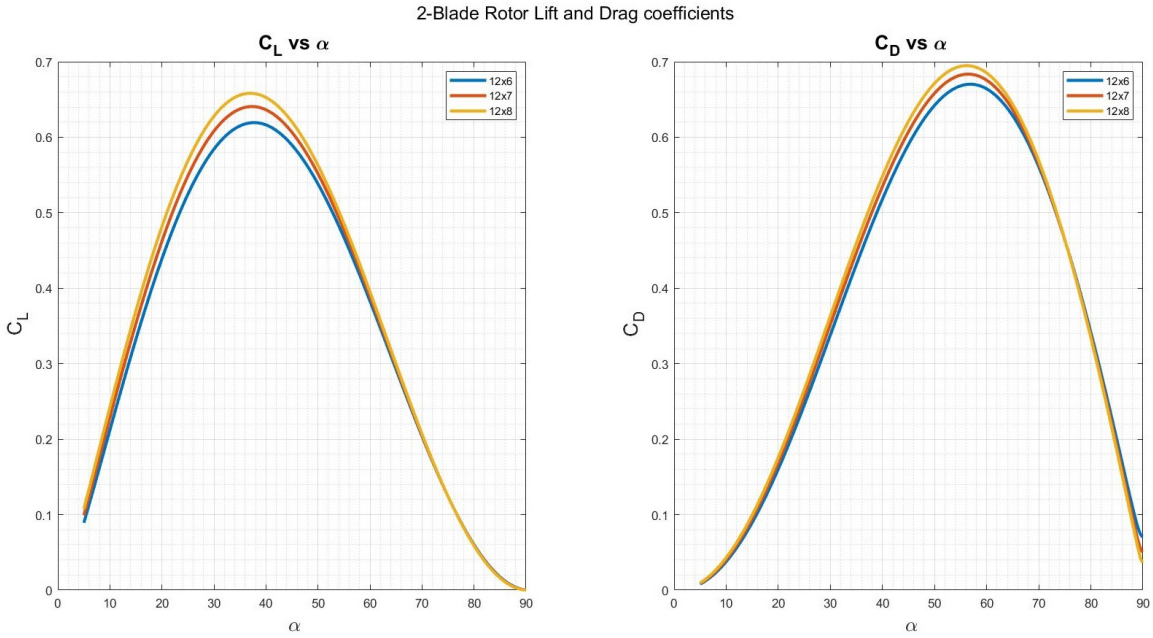

Figure 30. Analytical 2 Blade Coefficient of Lift and Drag

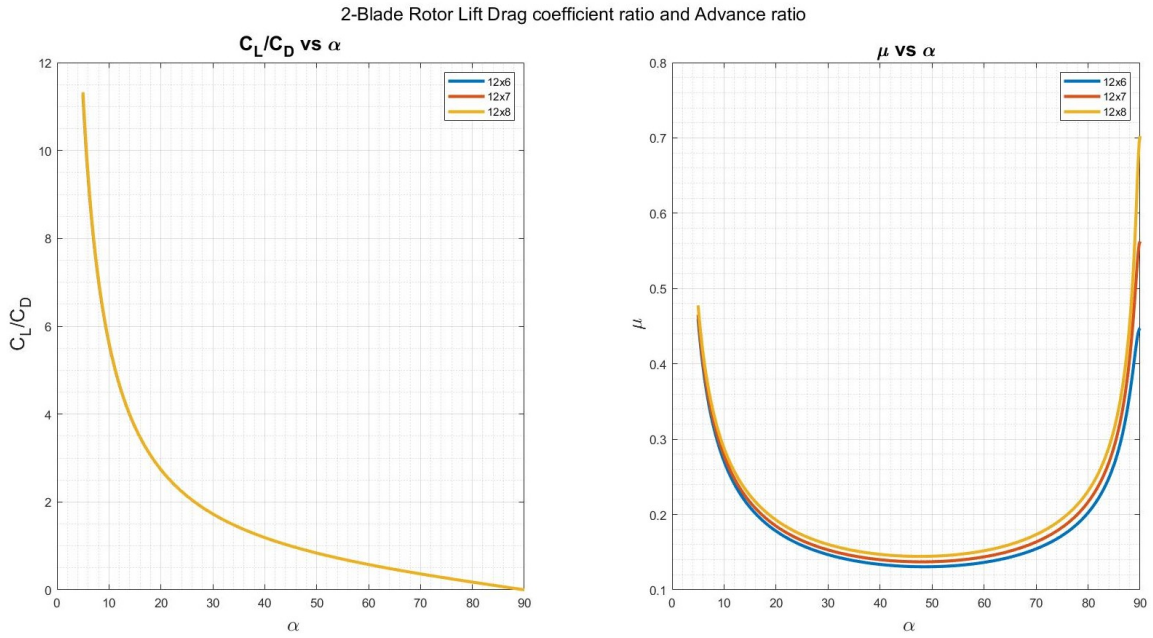

Figure 31. Analytical 2 Coefficient of Lift to Drag Ratio and Advance Ratio

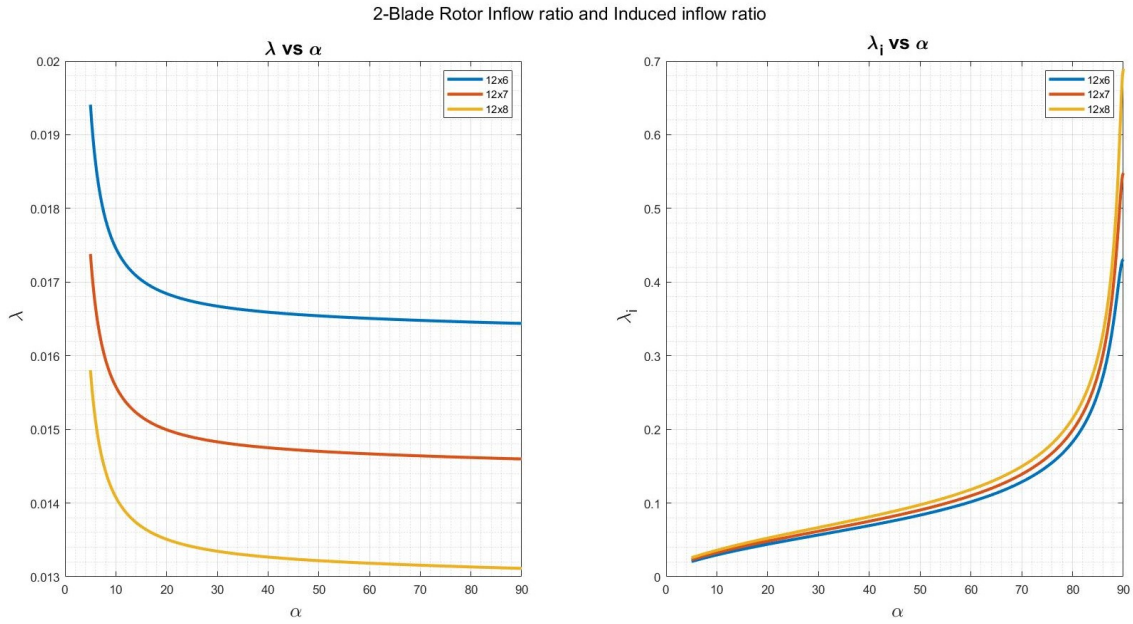

Figure 32. Analytical 2 Blade Inflow Ratio and Induced Inflow Ratio

4.2.2 3 Blade

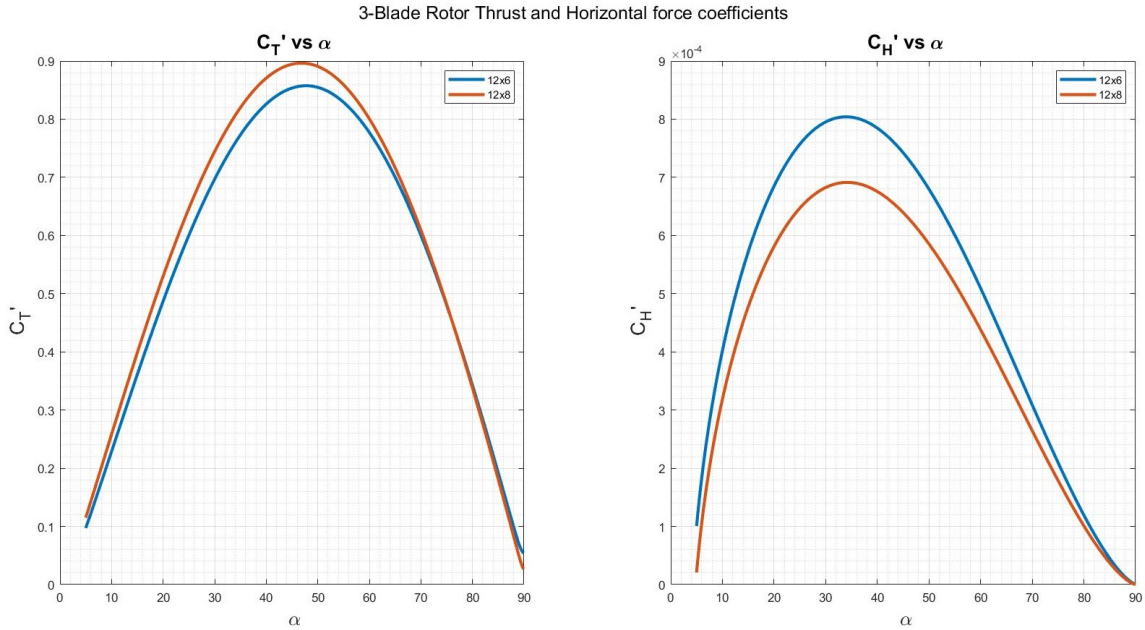

Figure 33. Analytical 3 Blade Coefficient of Thrust and Horizontal Force

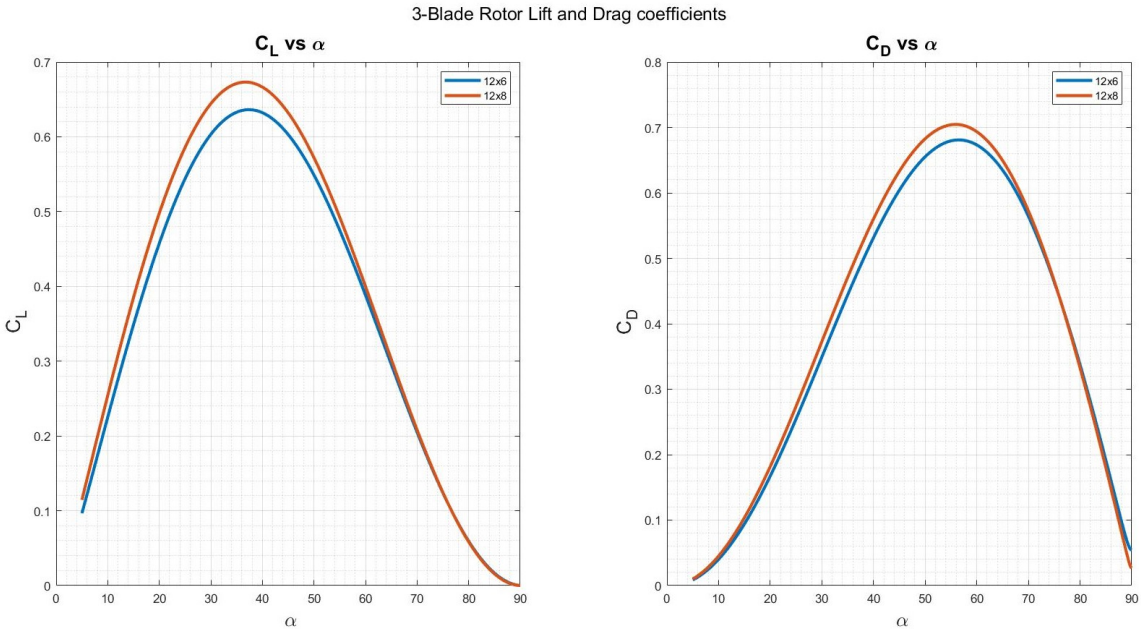

Figure 34. Analytical 3 Blade Coefficient of Lift and Drag

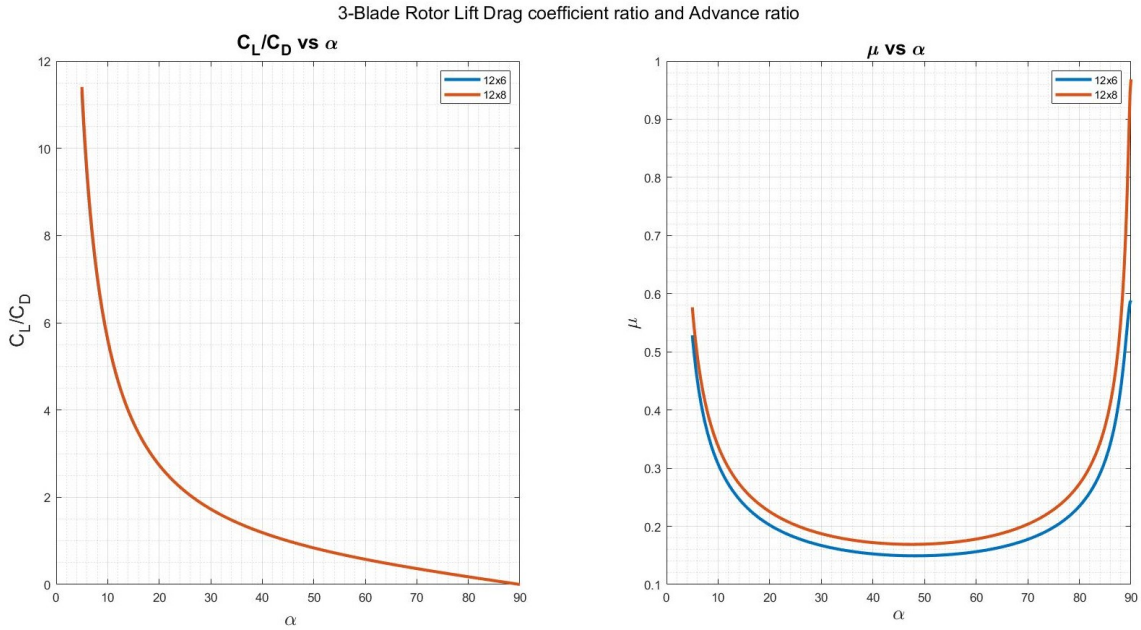

Figure 35. Analytical 3 Coefficient of Lift to Drag Ratio and Advance Ratio

Observing the plots in Figure 29 and Figure 33, the coefficient of thrust, lift and drag are observed to increase with pitch. The thrust coefficients are seen to be peaking between 45° and 50°. Whereas, the coefficients of lift peak between 35° and 40°. The

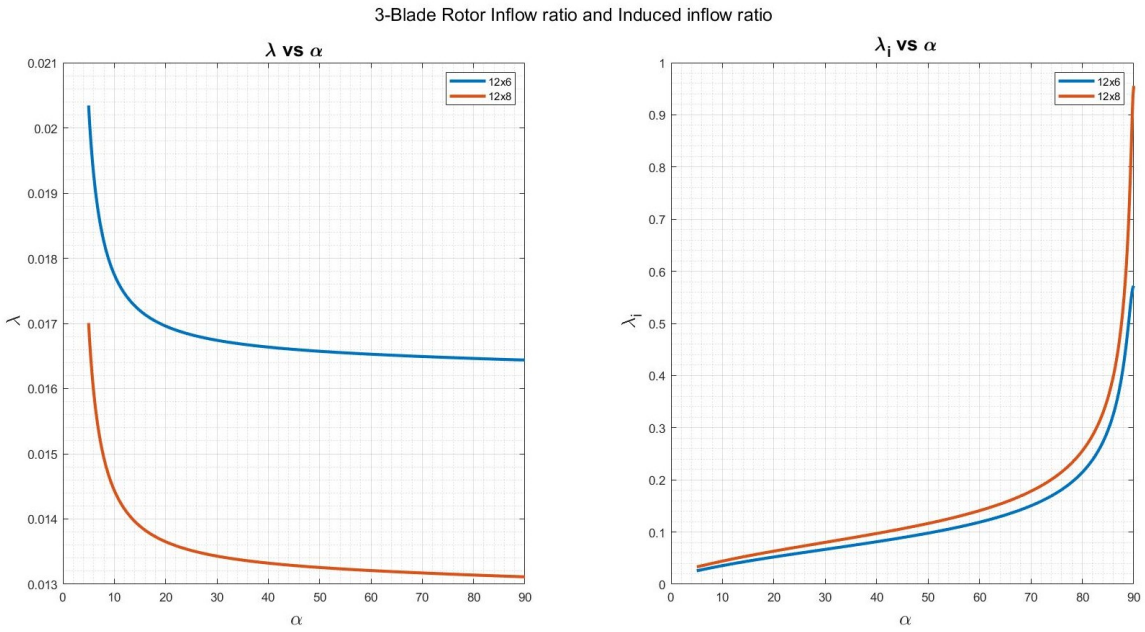

Figure 36. Analytical 3 Blade Inflow Ratio and Induced Inflow Ratio

maximum value for coefficient of drag is observed near 60°. On the contrary, the horizontal force coefficients are observed to decrease in magnitude with increasing pitch. Their peaks are observed at around a angle of 35°. The magnitudes of horizontal force are seen to be significantly smaller than the other forces.

As expected the ratio of lift to drag coefficients do not change with varying pitch. The advance ratio and induced inflow ratio vary very little with increasing pitch, but they are seen to increase with pitch. Over the interior range of angles, the advance ratio μ, remains relatively constant. The sudden increase near $\pi/2$ is unexpected, and the error could be attributed with the solver. The total inflow ratio λ tends to decrease with increasing pitch.

4.3 Experimental Results

4.3.1 2 Blade at $V_\infty \approx 11\ ms^{-1}$

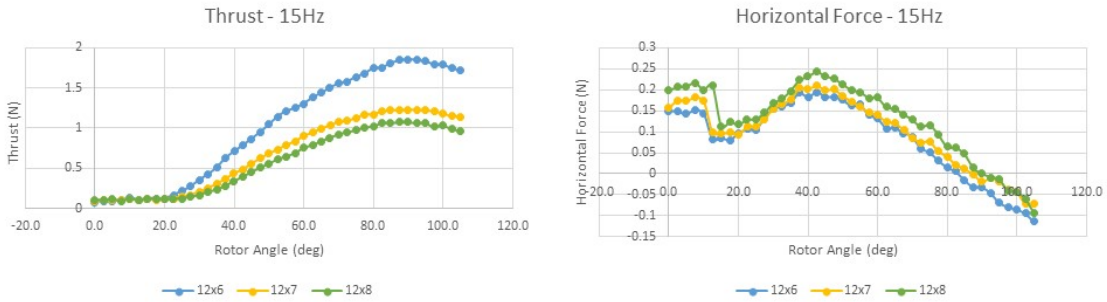

Figure 37. Experimental 2 Blade Thrust and Horizontal Force ($V_\infty \approx 11\ ms^{-1}$)

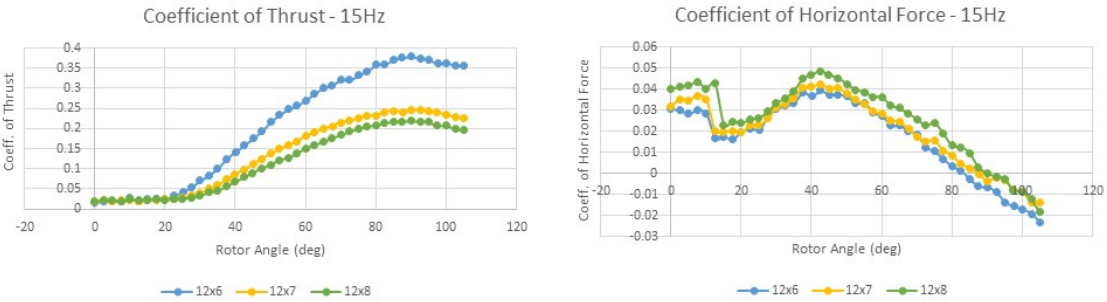

Figure 38. Experimental 2 Blade Coefficient of Thrust and Horizontal Force ($V_\infty \approx 11\ ms^{-1}$)

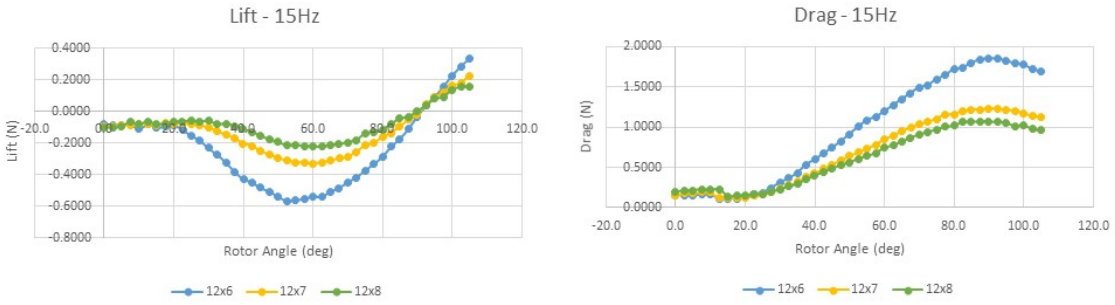

Figure 39. Experimental 2 Blade Lift and Drag ($V_\infty \approx 11\ ms^{-1}$)

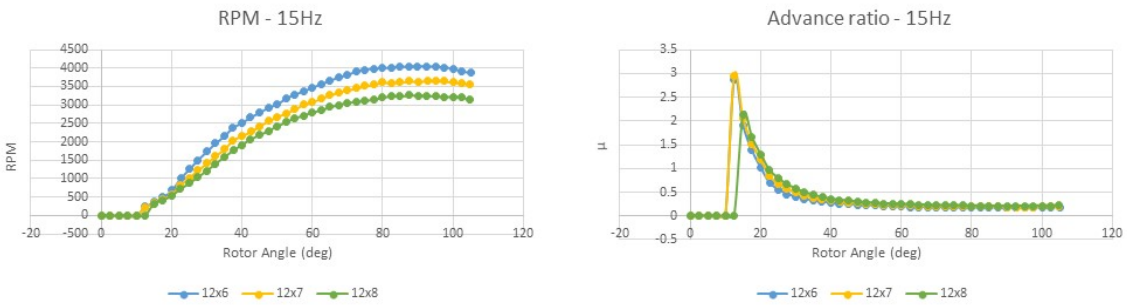

Figure 40. Experimental 2 Rotor speed and Advance Ratio ($V_\infty \approx 11\ ms^{-1}$)

4.3.2 2 Blade at $V_\infty \approx 14.9\ ms^{-1}$

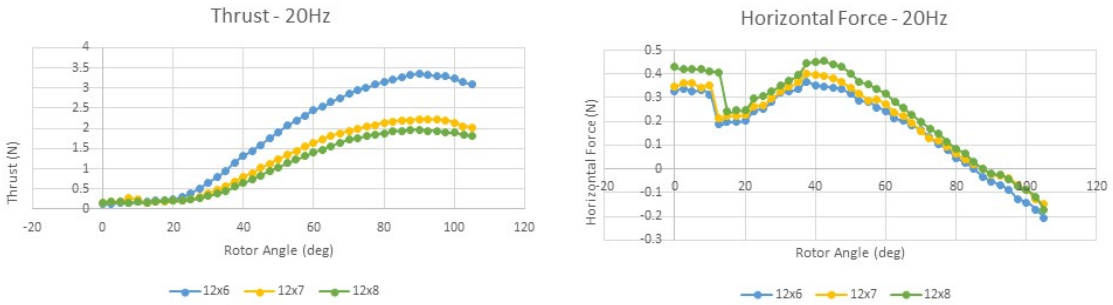

Figure 41. Experimental 2 Blade Thrust and Horizontal Force ($V_\infty \approx 14.9\ ms^{-1}$)

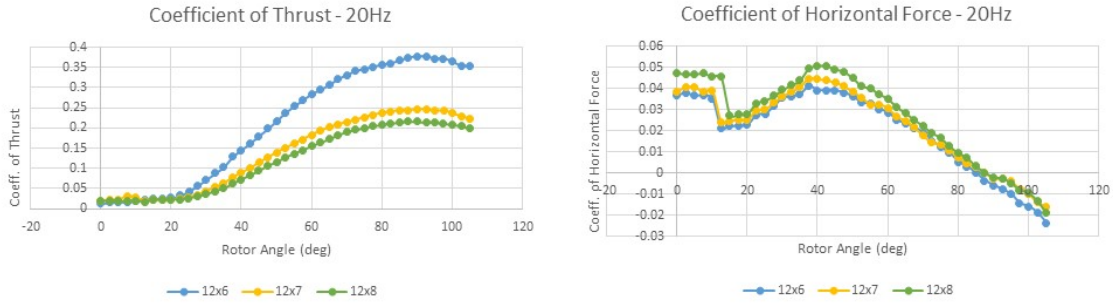

Figure 42. Experimental 2 Blade Coefficient of Thrust and Horizontal Force ($V_\infty \approx 14.9\ ms^{-1}$)

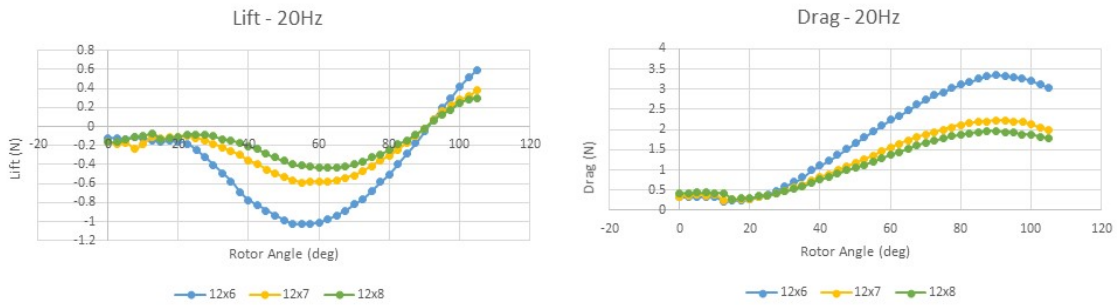

Figure 43. Experimental 2 Blade Lift and Drag ($V_\infty \approx 14.9\ ms^{-1}$)

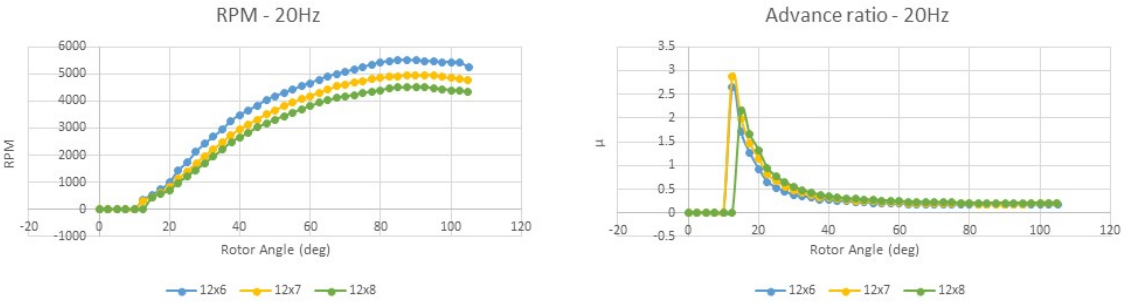

Figure 44. Experimental 2 Rotor Speed and Advance Ratio ($V_\infty \approx 14.9\ ms^{-1}$)

4.3.3 3 Blade at $V_\infty \approx 11\ ms^{-1}$

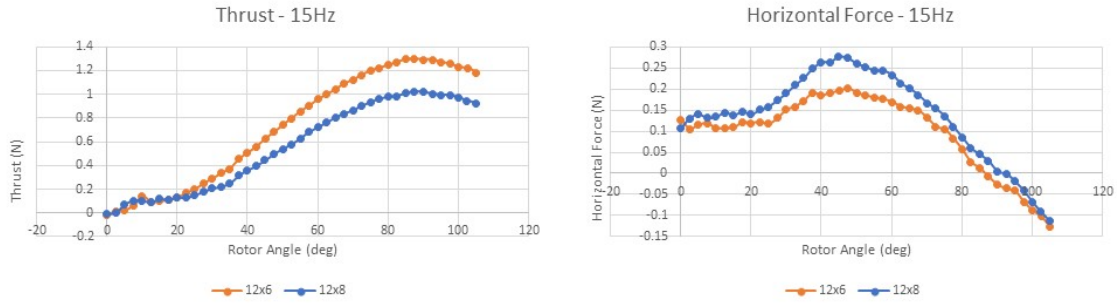

Figure 45. Experimental 3 Blade Thrust and Horizontal Force ($V_\infty \approx 11\ ms^{-1}$)

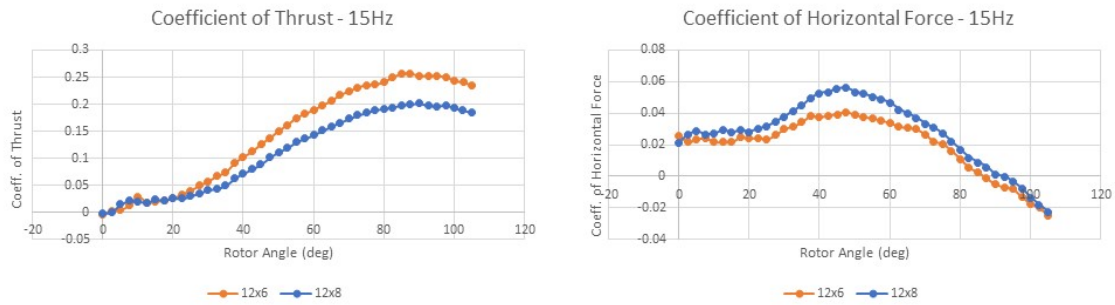

Figure 46. Experimental 3 Blade Coefficient of Thrust and Horizontal Force ($V_\infty \approx 11\ ms^{-1}$)

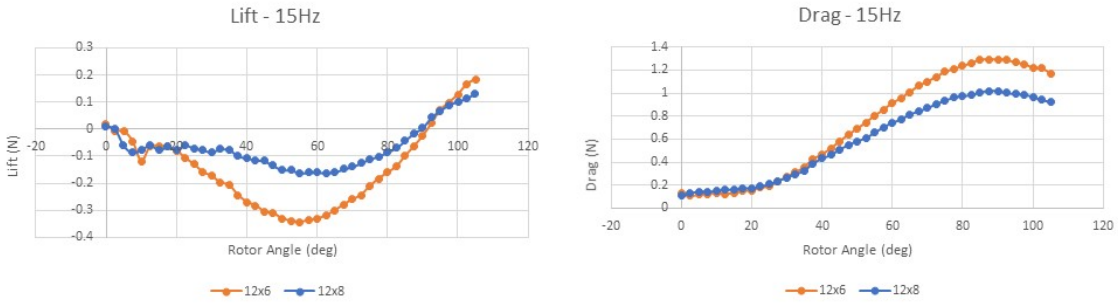

Figure 47. Experimental 3 Blade Lift and Drag ($V_\infty \approx 11\ ms^{-1}$)

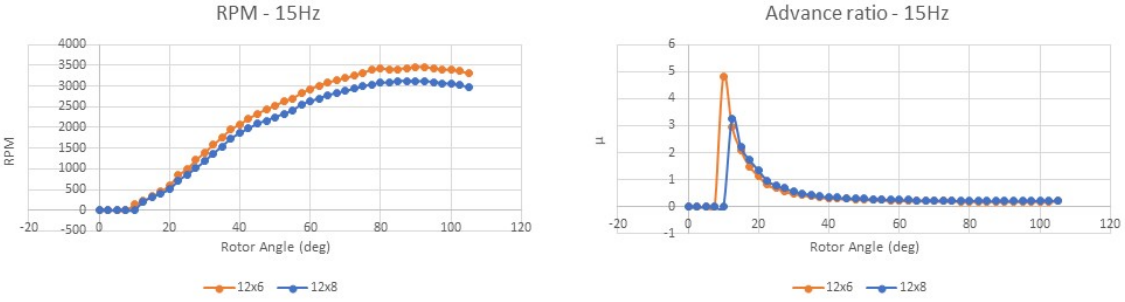

Figure 48. Experimental 3 Rotor Speed and Advance Ratio ($V_\infty \approx 11\ ms^{-1}$)

4.3.4 3 Blade at $V_\infty \approx 14.9\ ms^{-1}$

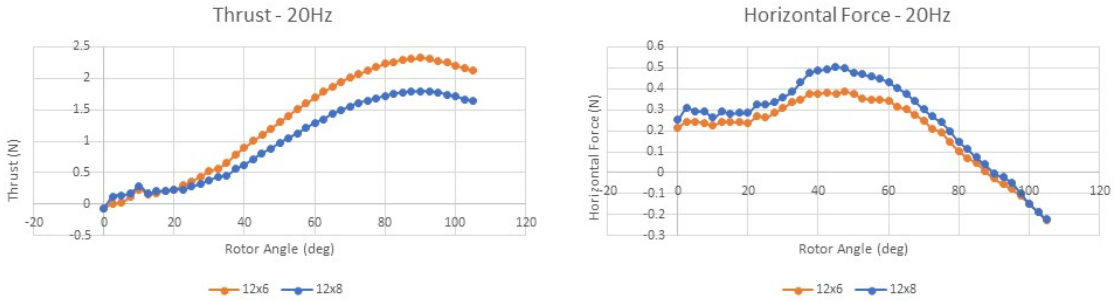

Figure 49. Experimental 3 Blade Thrust and Horizontal Force ($V_\infty \approx 14.9\ ms^{-1}$)

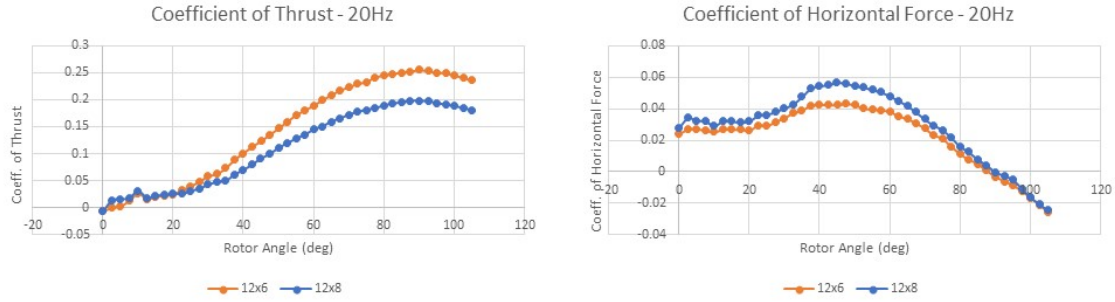

Figure 50. Experimental 3 Blade Coefficient of Thrust and Horizontal Force ($V_\infty \approx 14.9\ ms^{-1}$)

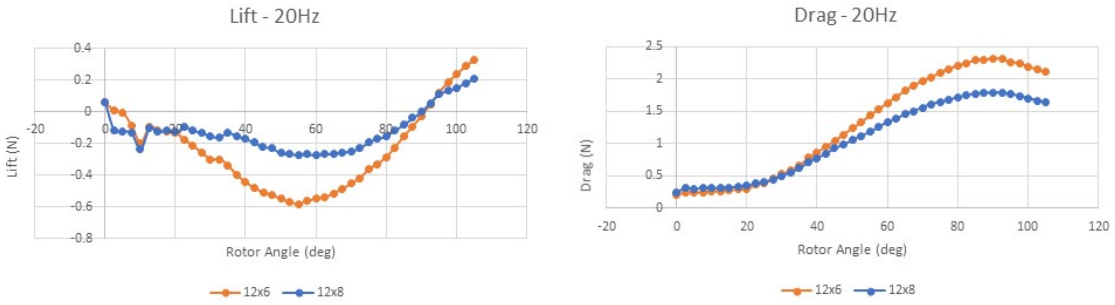

Figure 51. Experimental 3 Blade Lift and Drag ($V_\infty \approx 14.9\ ms^{-1}$)

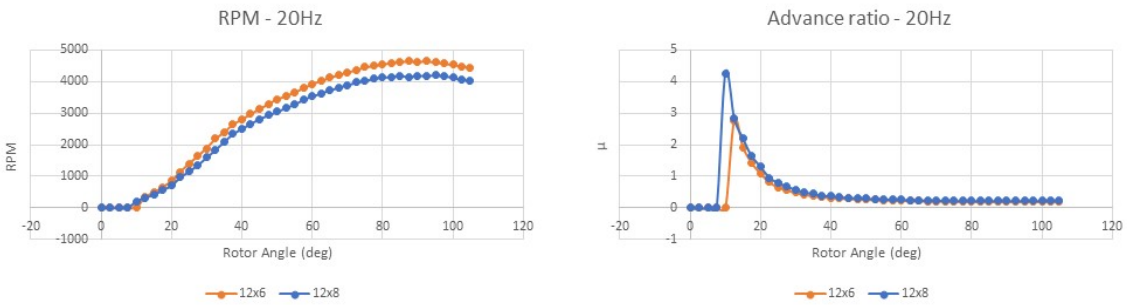

Figure 52. Experimental 3 Rotor Speed and Advance ratio ($V_\infty \approx 14.9\ ms^{-1}$)

4.3.5 Velocity Variations for 3 Blade 12×8 Propeller

The effect of velocity variations on the aerodynamic parameters have been observed to be similar for all rotors, hence the plots for only one rotor has been shown here. The forces can be non-dimensionalized based on the free stream velocity or by the tip speed of rotor. The plots of coefficients of thrust and horizontal force have been shown to be normalized with the free stream velocity, also with the tip speed (ΩR).

$$C_T = \frac{T}{\frac{1}{2}\rho A(V_\infty)^2} \qquad or \qquad C_T = \frac{T}{\frac{1}{2}\rho A(\Omega R)^2}$$

Similarly, the coefficient of horizontal force can be defined as,

$$C_H = \frac{H}{\frac{1}{2}\rho A(V_\infty)^2} \qquad or \qquad C_H = \frac{H}{\frac{1}{2}\rho A(\Omega R)^2}$$

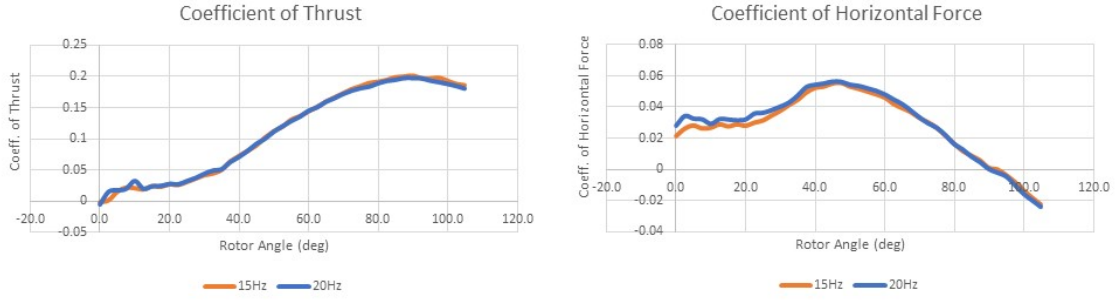

Figure 53. Experimental Coefficient of Thrust and Horizontal Force based on V_∞ (3 Blade - 12×8)

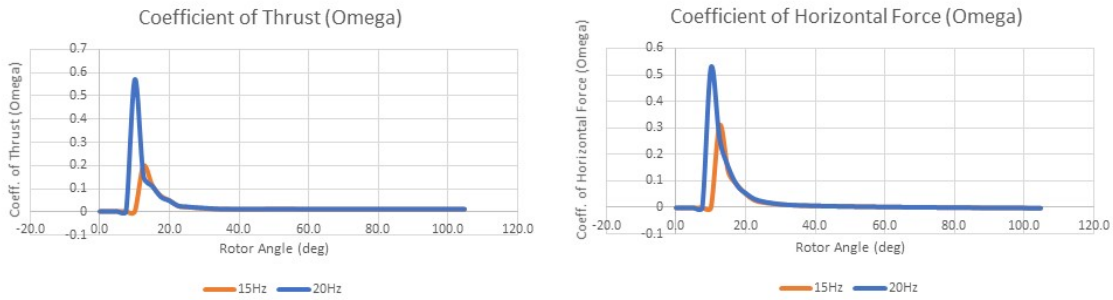

Figure 54. Experimental Coefficient of Thrust and Horizontal Force based on ΩR (3 Blade - 12×8)

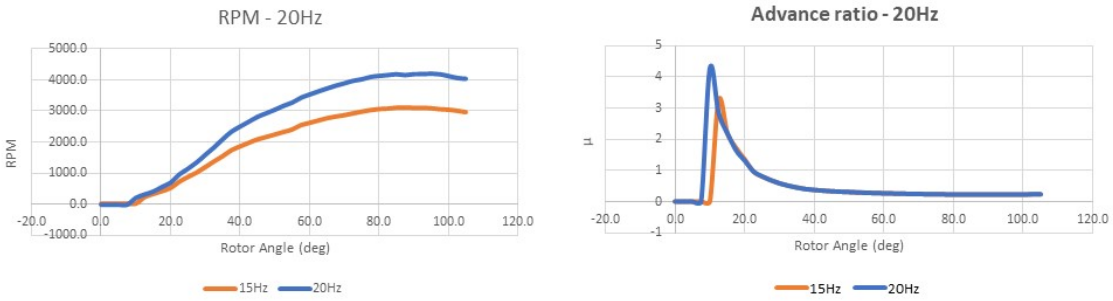

Figure 55. Experimental Rotor Speed and Advance Ratio (3 Blade - 12×8)

With respect the experimental analysis, it can be observed in Figures 37, 38, 41, 42, 45, 46, 49, and 50 the thrust tends to increase as rotor turns perpendicular to the flow. This could be said to be an expected result as at $\pi/2$, the rotor is perfectly normal to the flow. The thrust is observed to decrease with higher rotor pitch. The horizontal forces are observed to peak at an angle of 50°, contrary to thrust the H-force increases with increasing pitch.

As visualized on Figures 39, 43, 47, and 51, the magnitude of Lift and Drag tends to decrease with higher pitch. Lift is negative due to the orientation of rotor in the wind tunnel. The maximum lift is observed at about 60° rotor angle. The drag, similar to thrust is a maximum at $\pi/2$. With respect to Figures 40, 44, 48, and 52, the rotor angular speeds are observed to decrease with increasing pitch. The maximum

revolutions per minute is realized at and angle of $\pi/2$. The advance ratio tends to infinity near when the rotor is parallel to the flow, since there are no rotations, and ΩR is zero. The plots do not include the tendency of going to infinity, hence show no values.

On comparing the variations of velocity, as in Figure 53, the coefficient of thrust and H-force do not change with velocity. The coefficients are independent of the free stream velocity when non-dimensionalized with the free stream velocity. On non-dimensionalizing the forces with the tip speed it is observed that after a particular rotor plane angle α, the coefficients stabilize at a constant value. These coefficients are not zero but are very small in magnitude, hence not clearly visible on the plots. On studying Figure 55, we can see a very common trend of the angular velocity increasing with the free stream velocity. The advance ratio is seen to independent of the free stream velocity, as with higher velocities the angular speed is also increasing. On non-dimensionalizing the free stream velocity with the tip velocity, it basically breaks down to the same magnitudes of advance ratio.

4.4 Analysis

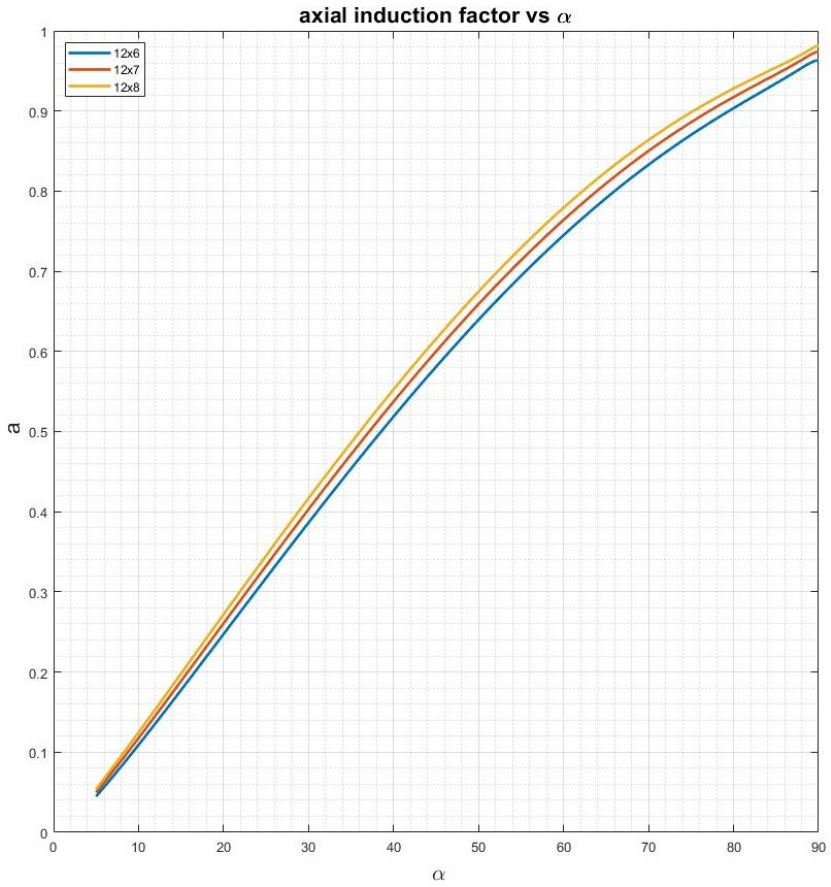

Figure 56. Analytical Axial Induction Factor 2-Bladed

On comparing the analytical results to the experimental one, the coefficients of thrust, and drag have a similar plot trend till a rotor plane angle of about 45°. Past that angle, we expect the thrust and drag to keep on increasing till 90°, but in the analytical model the thrust and drag coefficients drop. To investigate further, the axial induction factor was computed for different angles. The plot in Figure 56 depicted that axial induction factor was greater than 1/2 for angles higher than about 40°. Additionally a plot of C_T vs α shown in Figure 57, for the analytical model showed a very similar behavior to Figure 5. At higher angles, the rotor can seen to enter into the turbulent wake state where we have known that the momentum theory does not

hold valid. Whereas, the analytical model in this thesis used the fourth order induced velocity equation which was derived from the momentum theory. At higher angles, the relationship of induced velocity from momentum theory becomes invalid, and thus explains the discrepancy in the trend from the analytical model.

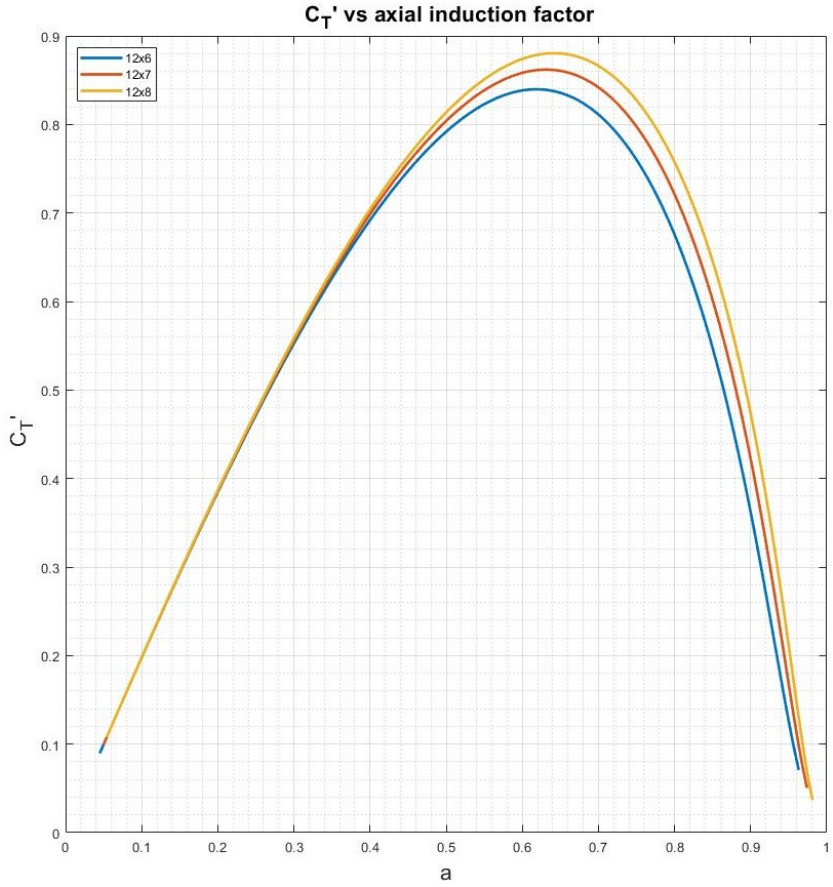

Figure 57. Analytical C_T vs Axial Induction Factor 2-Bladed

To directly compare the rotor force coefficients, the analytical and experimental plots are overlapped. The results are just shown for the 12×7 propeller. At lower angles, the trends for thrust can be seen to be similar as in Figure 59. But the magnitudes of the coefficients are very different. To investigate further, the thrust and horizontal force coefficients based on ΩR were plotted. They also show a similarity in

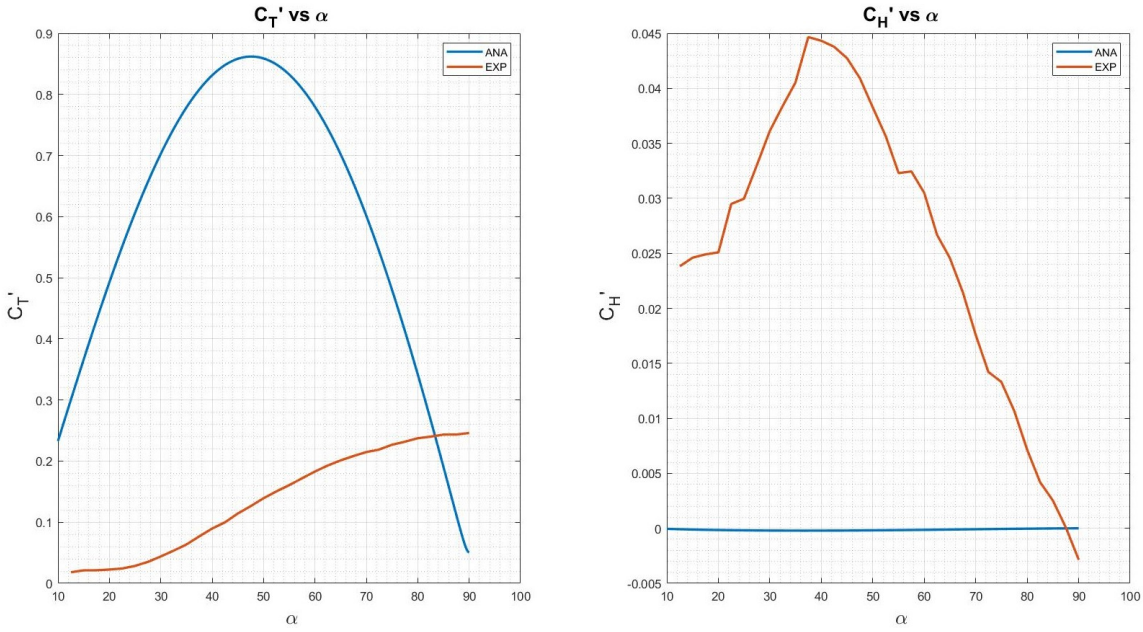

Figure 58. Thrust Coefficient vs Angle (2 Blade - 12×7)

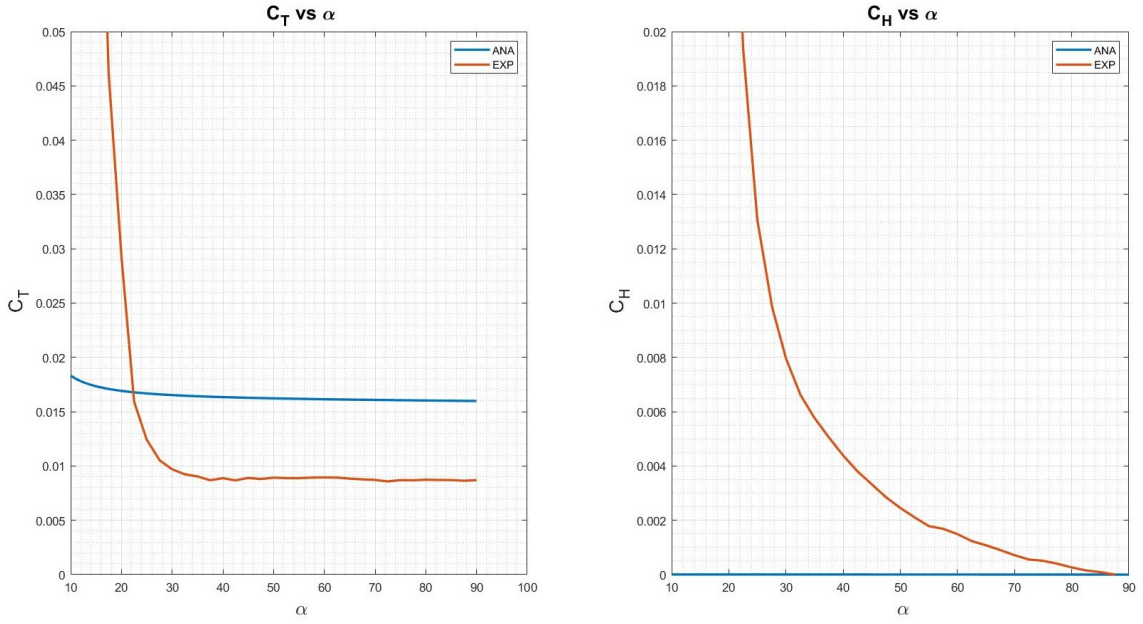

Figure 59. Thrust Coefficient based on Tip Speed vs Angle (2 Blade - 12×7)

trend but variation in magnitude. The analytical model is observed to over-estimate the coefficients by a huge margin. This inaccuracy is thought to be coupled with the assumptions of aerodynamic constants such as the pitch angle at 75% of blade, twist, lift curve slope, and airfoil coefficient of drag. These constants have a significant

relation to the calculated force coefficients. Due to the lack of available data, these constants were needed to be assumed. This is thought to be the primary reason behind the discrepancies in magnitude.

The horizontal force coefficients, estimated by the analytical model are almost negligible compared to the experimental values. The horizontal forces are dependent on the flow interactions due to flapping, radial velocity, etc., which are not considered in this model. Especially, the horizontal force is affected by reverse flow regions, which is unaccounted for in the analytical analysis. Horizontal force is usually difficult to predict, and will need a refined model considering various flow interactions.

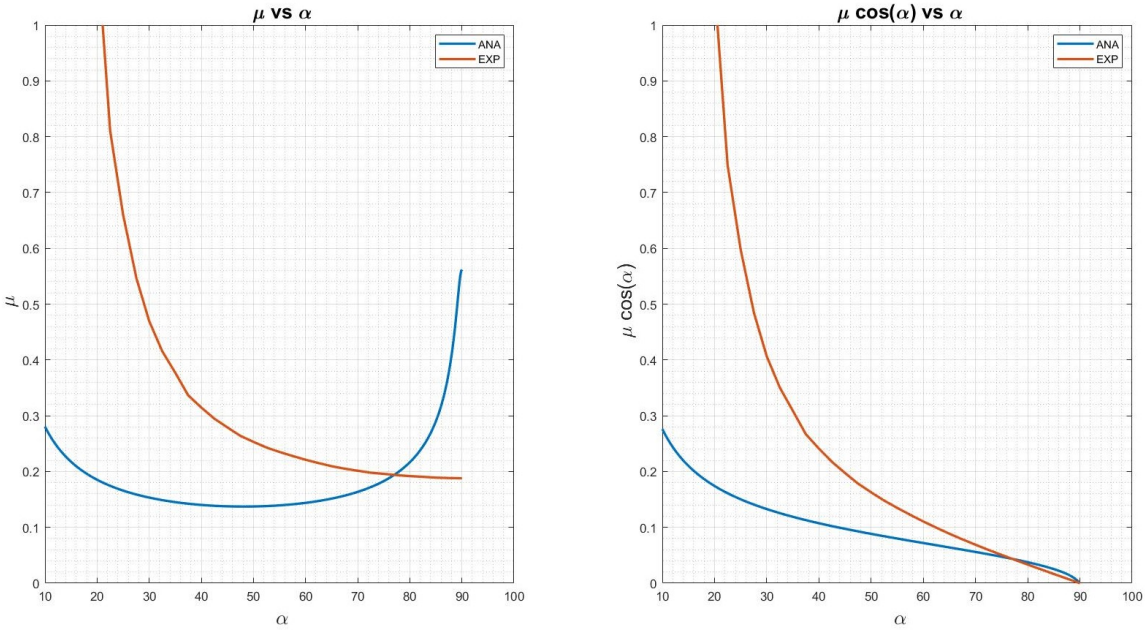

Figure 60. Advance Ratio vs Angle (2 Blade - 12×7)

Lastly, to understand characteristics, the advance ratio and advance ratio times cosine of rotor angle was plotted (Figure 60) for various angles of attack. Firstly it is observed that the analytical model blows up near 90°. Secondly the experimental advance ratio is observed to be significantly higher than the analytical model. The second observation suggests an important idea - the rotor might be rotating slower than it is expected, yielding a higher advance ratio. On contemplating, in reality it is

not possible that we would have a ideal torque free case. In the experiment, due to friction there surely will be some losses. The bearing's friction loss is highly influenced by the tightening torque of the propeller constraining bolt and the rotational velocity of the bearing. The analytical model did not account for these torque losses, which can be a major setback to the analytical analysis.

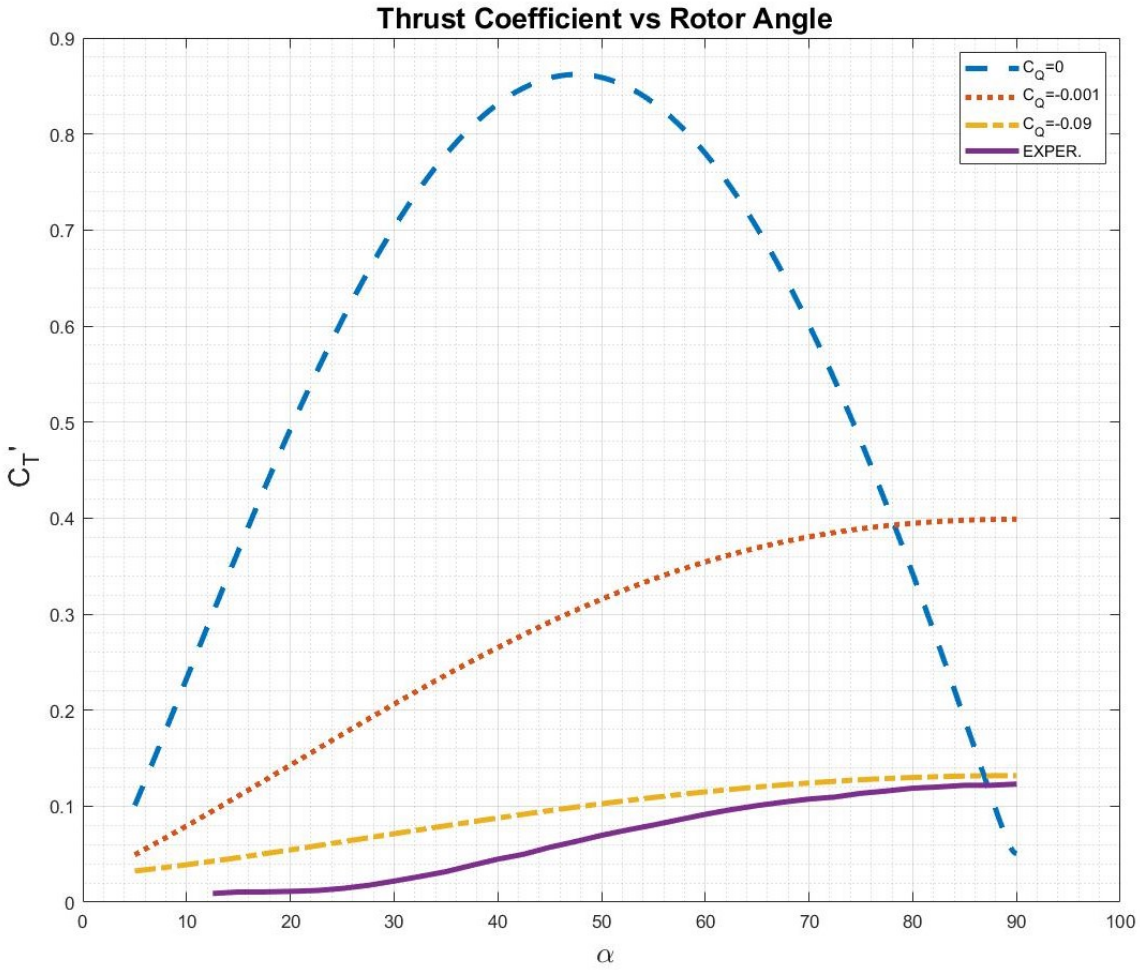

Figure 61. Thrust Coefficient Variation Accounting for Torque Loss (2 Blade - 12×7)

To further expand on the previous idea, the analytical model was introduced with a torque loss coefficient. The graph (Figure 61) shows results for the thrust coefficient ($C_T{}'$) from the analytical model for three different values of constant torque (zero, small and medium values) along with the experimental data for the 2-bladed

12x7 propeller. A zero-torque rotor operating in this configuration is in a state of ideal vertical autorotation where the momentum theory is not valid. However, introducing just a small resisting torque completely alters the character of the curve; the thrust produced continues to increase up to $\alpha = 90^\circ$ as expected and as measured experimentally. Further increasing the resisting torque results in a curve much closer to the actual data acquired in the wind tunnel. The real amount of resisting torque depends on the bearing design and even how tightly the propeller is bolted onto the mount, so the actual value is currently unknown. However, it is clear that any realistic analysis should not make the assumption that the rotor is operating in the torque-free state.

Chapter 5

CONCLUSION

The dependencies of an autorotating rotor on its pitching angle can be significantly affect its performance. An analytical model estimating the aerodynamic performance parameters can essentially provide a guideline for design. The research here aimed to develop a relatively simple but effective model for autorotation confirmed by an experimental analysis.

By examining the wind tunnel propeller free-wheeling test data, it can be stated that the thrust, drag and angular velocity increase with the pitch angle, and have a maximum value when the rotor is perpendicular to the flow. The lift and horizontal force are seen to be highest at nearly 50°, and 40° respectively. The increase in blade pitch decreases the thrust, lift and drag.

By analyzing the thrust and drag coefficients, this thesis has shown experimentally the thrust should increase with increasing rotor plane angle of attack. Analytically when torque is set to zero we see differently as, the rotor tends to operate in the turbulent wake and vortex ring zone when highly pitched. In such operating states, a different model needs to be developed without dependencies on the momentum theory. But more importantly we note that, in reality we do not have a torque free case. A slight loss of torque when modelled into the analytical analysis changes the nature of graph significantly. A comparably medium value of torque loss coefficient shows close match to experimental results. Furthermore, the lack of inclusion of actual blade airfoil data, results in a poorly estimated magnitude of force coefficients. The blade characteristics are highly sensitive to constants like lift curve slope, coefficient of drag, blade twist and solidity. It is necessary to accurately determine this data for persuasive comparison.

To better understand the implications of these results, future research should incorporate accurate values for the experimental torque loss coefficients into the analytical model. It should also aim to develop an enhanced analytical model for horizontal force coefficients considering reverse flow regions. The aerodynamic constants used in the analytical model will need to be determined accurately for the rotor under analysis.

Applications of airborne wind turbines and unconventional turbines like Cierva rotor wind turbine, have rotors that are highly pitched to the oncoming flow. The underlying aerodynamics of such rotors, must be investigated to design efficient systems. Notwithstanding the inherent challenges of aerodynamic modelling of highly pitched auto-rotating rotors, a clear need for accurate estimation of forces is needed for the design and dynamic analysis, since available autogyro models can only estimate with confidence the forces for relatively low pitching angles.

REFERENCES

[1] American Wind Energy Association. *Wind Facts at a Glance*. URL: https://www.awea.org/wind-energy-facts-at-a-glance.

[2] WindExchange. *Wind Energy Maps and Data*. URL: https://windexchange.energy.gov/maps-data?category=residential.

[3] D. Gerrard. *High Altitude Tethering of Wind Turbines*. URL: http://large.stanford.edu/courses/2014/ph240/gerrard1/.

[4] B. W. Roberts, D. H. Shepard, K. Caldeira, M. E. Cannon, et al. 'Harnessing High-Altitude Wind Power'. In: *IEEE Transactions on Energy Conversion* 22.1 (2007), pp. 136–144.

[5] J. G. Leishman. *Principles of helicopter aerodynamics*. New York, NY: Cambridge University Press, 2005.

[6] R. Hafner, ed. *Rotor Systems and Control Problems of Helicopters*. 1947.

[7] C. Lock. *Note on the characteristic curve for an airscrew or helicopter*. Reports and memoranda. H.M. Stationery Office, 1952.

[8] A. Gessow. *Review of information on induced flow of a lifting rotor*. Washington: NACA, 1954.

[9] D. M. Eggleston and F. S. Stoddard. *Wind turbine engineering design*. New York: Van Nostrand Reinhold, 1987.

[10] Sven Schmitz. *Wind Turbine Aerodynamics: The Actuator Disk Model*. URL: https://www.e-education.psu.edu/aersp583/node/514.

[11] H. Glauert. *The analysis of experimental results in the windmill brake and vortex ring states of an airscrew*. London: HMSO, 1926.

[12] C. N. H. Lock, H. Bateman, and H. C. Townend. *An extension of the vortex theory of airscrews with applications to airscrews of small pitch, including experimental results*. HM Stationery Office, 1926.

[13] M. L. Buhl Jr. *New empirical relationship between thrust coefficient and induction factor for the turbulent windmill state*. 2005.

[14] H. Glauert. *A general theory of the autogyro*. London: HMSO, 1928.

[15] J. B. Wheatley. 'An Aerodynamic analysis of the autogiro rotor with a comparison between calculated and experimental results'. In: (1935).

[16] D. Seter and A. Rosen. 'Theoretical and Experimental Study of Axial Autorotation of Simple Rotary Decelerators'. In: *Journal of Aircraft Journal of Aircraft* 51.1 (2014), pp. 236–248.

[17] S. Rimkus, T. Das, Annual Conference, and 6th. 'An Application of the Autogyro Theory to Airborne Wind Energy Extraction'. In: (2013).

[18] J. A. Kentfield and D. C. Brophy. 'The predicted performance of Cierva-rotor wind turbines'. In: *windengi Wind Engineering* (1997), pp. 89–101.

[19] J. B. Wheatley, United States., and National Advisory Committee for Aeronautics. *The Aerodynamic analysis of the gyroplane rotating-wing system.* Washington D.C.: National Advisory Committee for Aeronautics, 1934.

[20] N. Kostreski. *Educational Wind Tunnel.* Aerolab, 2016.

APPENDIX A

MATLAB CODE TO SOLVE MODEL WITH TWIST

```
clc
clear all
alpha=linspace(2*pi/180,pi/2,500);
guess = [0.0137 0.1270];

options = optimset('MaxIter',1000000,'MaxFunEval',1000000);

theta_75 = 2*pi/180; %Theta at 75% of blade
theta_tw = -5*pi/180; %Twist angle
C_la=6; %Lift curve slope
C_d = 0.006 ; %Assuming coeff of Drag
sigma = 0.2; %Assuming Solidity

constants=[theta_75 theta_tw C_la C_d sigma];

lambda=zeros(1,length(alpha));
mu=zeros(1,length(alpha));
C_H=zeros(1,length(alpha));
C_T=zeros(1,length(alpha));

for i=1:1:length(alpha)
    if i>1
        guess=y;
    end
    y=fsolve(@(x) rotorfixedpitch(x,constants,alpha(i)),guess,
   options);
    lambda(i)=y(1);
    mu(i)=y(2);

    C_T(i)= 1/48 * sigma*(C_la*(8*theta_75 ...
        + 12*theta_75*(mu(i)*cos(alpha(i)))^2 ...
    -3*theta_tw*(mu(i)*cos(alpha(i)))^2 + 12*lambda(i))+12*C_d*
   lambda(i));
    C_H(i)= 1/16 * sigma*mu(i)*cos(alpha(i))...
        *(4*C_d-4*theta_75*C_la*lambda(i)+theta_tw*C_la*lambda(i));
end

C_T2=C_T./mu.^2;
C_H2=C_H./mu.^2;

C_L=C_T2.*cos(alpha) - C_H2.*sin(alpha);
C_D=C_T2.*sin(alpha) + C_H2.*cos(alpha);
C_LD_ratio=C_L./C_D;

figure()
subplot(2,2,1)
plot (alpha*180/pi,C_T,'LineWidth',1.5)
grid on
grid minor
title('C_{T} vs \alpha'),...
    xlabel('\alpha'), ylabel('C_{T}')

subplot(2,2,2)
plot (alpha*180/pi,C_H,'LineWidth',1.5)
```

```
grid on
grid minor
title('C_{H} vs \alpha'),...
    xlabel('\alpha'), ylabel('C_{H}')

subplot(2,2,3)
plot (alpha*180/pi,C_T2,'LineWidth',1.5)
grid on
grid minor
title('C_{T}'' vs \alpha'),...
    xlabel('\alpha'), ylabel('C_{T}''')

subplot(2,2,4)
plot (alpha*180/pi,C_H2,'LineWidth',1.5)
grid on
grid minor
title('C_{H}'' vs \alpha'),...
    xlabel('\alpha'), ylabel('C_{H}''')

subplot(3,3,5)
plot (alpha*180/pi,mu,'LineWidth',1.5)
grid on
grid minor
title('\mu vs \alpha '),...
    xlabel('\alpha'), ylabel('\mu')

subplot(3,3,6)
plot (alpha*180/pi,lambda,'LineWidth',1.5)
grid on
grid minor
title('x vs \alpha '),...
    xlabel('\alpha'), ylabel('\lambda')

subplot(3,3,7)
plot (alpha*180/pi,C_L,'LineWidth',1.5)
grid on
grid minor
title('C_{L} vs \alpha'),...
    xlabel('\alpha'), ylabel('C_{L}')

subplot(3,3,8)
plot (alpha*180/pi,C_D,'LineWidth',1.5)
grid on
grid minor
title('C_{D} vs \alpha'),...
    xlabel('\alpha'), ylabel('C_{D}')

subplot(3,3,9)
plot (alpha*180/pi,C_LD_ratio,'LineWidth',1.5)
grid on
grid minor
title('C_{L}/C_{D} vs \alpha '),...
    xlabel('\alpha'), ylabel('C_{L}/C_{D}')
sgtitle('Thesis Model with linear twist')
```

```
function out=rotorfixedpitch(x,constants,alpha)
lambda=x(1);
mu=x(2);

theta_75=constants(1);
theta_tw=constants(2);
C_la = constants(3);
C_d = constants(4);
sigma = constants(5);

out(1)=mu*sin(alpha)-(1/48 * sigma*(C_la*(8*theta_75 ...
    + 12*theta_75*(mu*cos(alpha))^2-3*theta_tw*(mu*cos(alpha))^2 ...
    + 12*lambda)+12*C_d*lambda))/(2*sqrt((mu*cos(alpha))^2+lambda^2)
   )-lambda;
out(2)=3*C_d*((mu*cos(alpha))^2 + 1)-2*C_la*(2*theta_75*lambda+3*
   lambda^2);
end
```

APPENDIX B

MATLAB CODE TO SOLVE GLAURET'S MODEL

```
clear all
clc

guess1 = [0.01 0.01 0.01 ];

theta = 2*pi/180; % Assuming average Coeff of Lift
delta = 0.006 ; %Assuming coeff of Drag
sig = 0.2; %Assuming Solidity

y=fsolve(@(unkn1) set1(unkn1,theta,delta,sig),guess1,[]);
x=y(1);
T_c=y(2);
zeta=y(3);

alpha=linspace(2*pi/180,pi/2,500);

H_c=zeros(length(alpha),1);
Lamcosi=zeros(length(alpha),1);
mew=zeros(length(alpha),1);
k_z=zeros(length(alpha),1);
k_x=zeros(length(alpha),1);

guess2=0.01;
guess3=[0.01 0.01];
for j=1:1:length(alpha)
    if j>1
        guess2=Lamcosi(j-1);
        guess3=y;
    end

fun=@(Lam_cos_i) (Lam_cos_i.*tan(alpha(j)) - x) ...
    - ((0.5*T_c)./sqrt((Lam_cos_i).^2 + x^2));
Lamcosi(j)=fzero(fun,guess2);

mew(j)= Lamcosi(j)/cos(alpha(j));
H_c(j) = sig*zeta*Lamcosi(j);

y=fsolve(@(unkn3) set3(unkn3,alpha(j),Lamcosi(j),T_c,H_c(j)),guess3
   ,[]);
k_z(j)=y(1);
k_x(j)=y(2);
end

for i=1:length(k_x)
C_T(i)=k_x(i)*sin(alpha(i))+k_z(i)*cos(alpha(i));
C_H(i)=-k_z(i)*sin(alpha(i))+k_x(i)*cos(alpha(i));
end
kz_kx=k_z./k_x;

figure()
subplot(2,2,1)
plot (alpha*180/pi,k_z,alpha*180/pi,C_L,'LineWidth',2)
grid on
```

```
grid minor
legend('Glauret''s','Thesis, -5^{\circ} twist','Location','northwest
   ')
hTitle=title('C_{L} vs \alpha'),...
    xlabel('\alpha'), ylabel('C_{L}')
set(hTitle,'FontSize',20)

subplot(2,2,2)
plot (alpha*180/pi,k_x,alpha*180/pi,C_D,'LineWidth',2)
grid on
grid minor
legend('Glauret''s','Thesis, -5^{\circ} twist','Location','northwest
   ')
hTitle=title('C_{D} vs \alpha'),...
    xlabel('\alpha'), ylabel('C_{D}')
set(hTitle,'FontSize',20)

subplot(2,2,3)
plot (alpha*180/pi,mew,alpha*180/pi,mu,'LineWidth',2)
grid on
grid minor
legend('Glauret''s','Thesis, -5^{\circ} twist')
hTitle=title('\mu vs \alpha '),...
    xlabel('\alpha'), ylabel('\mu')
set(hTitle,'FontSize',20)

subplot(2,2,4)
plot (alpha*180/pi,kz_kx,alpha*180/pi,C_LD_ratio,'LineWidth',2)
grid on
grid minor
legend('Glauret''s','Thesis, -5^{\circ} twist')
hTitle=title('C_{L}/C_{D} vs \alpha'),...
    xlabel('\alpha'), ylabel('C_{L}/C_{D}');
set(hTitle,'FontSize',20)


function y1=set1(unkn1,theta,delta,sig)
x=unkn1(1);
T_c=unkn1(2);
zeta=unkn1(3);

y1(1) = delta - 4*x*(theta+(3*x)/2);
y1(2) = T_c - (sig*delta)/(4*x);
y1(3) = zeta-(8*theta^2)/3 - (17*theta*x)/2 - (15*x^2)/2;
end

function y3 = set3(unkn3,i,Lam_cos_i,T_c,H_c)
k_z=unkn3(1);
k_x=unkn3(2);

y3(3) = (Lam_cos_i/cos(i))^2 * k_z - T_c*cos(i)+H_c*sin(i);
y3(4) = (Lam_cos_i/cos(i))^2 * k_x - T_c*sin(i)-H_c*cos(i);
end
```